LANGMUIR

pubs.acs.org/Langmuir Article

Lyotropic Liquid Crystalline Phase Behavior of Boron Nitride Nanotube Aqueous Dispersions

Joe F. Khoury, Asia Matatyaho Ya'akobi, Alina Chow, Eldar Khabushev, Irina Davidovich, Davide Cavuto, Mingrui Gong, Lyndsey R. Scammell, Cheol Park, Yeshayahu Talmon, Angel A. Martí, and Matteo Pasquali*

Cite This: *Langmuir* 2025, 41, 15270−15282 Read Online

ACCESS | Metrics & More | Article Recommendations | Supporting Information

ABSTRACT: Boron nitride nanotubes (BNNTs) are gaining significant interest due to their outstanding mechanical and thermal properties, as well as their potential to serve as a model nanorod system. Processing BNNT liquid crystalline (LC) dispersions enables precise control over BNNT orientation in macroscopic assemblies, while their low absorption in the visible spectrum facilitates studying LCs at exceptionally high concentrations. Here, we investigate the behavior of BNNTs in aqueous solutions stabilized by the surfactant sodium deoxycholate (SDC), examining the effect of BNNT purity and BNNT−SDC concentrations on lyotropic LC formation. We disperse up to 15 wt % BNNT in SDC solutions and use polarized light microscopy to detail the transition from an isotropic state to a biphasic regime, where isotropic and nematic domains coexist due to phase separation, to a single fully nematic phase. Cryogenic electron microscopy provides direct evidence of BNNT alignment within nematic domains. Our results show that enhanced depletion-induced attractions, driven by increased surfactant concentration, lower the threshold concentration of BNNT required to form nematic domains. In contrast, low surfactant concentrations relative to BNNT result in insufficiently coated nanotube surfaces, leading to poor dispersions and BNNT aggregation. Additionally, we fabricate well-aligned BNNT films from aqueous LC dispersions. Our findings advance the understanding of BNNT LCs, offering insight into controlling their orientation and highlighting their potential for high-performance materials.

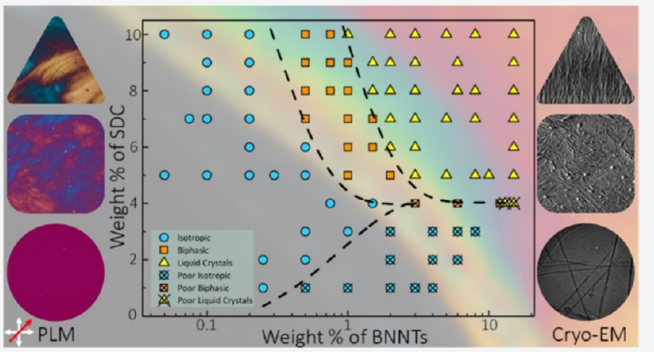

INTRODUCTION

Boron nitride nanotubes (BNNTs) are electrically insulating[1,2] lightweight nanoscale building blocks with outstanding mechanical[3] and thermal[4−6] properties.[7] Structurally, BNNTs can be conceptualized as tubular structures, reminiscent of carbon nanotubes (CNTs), obtained by rolling a hexagonal boron nitride (h-BN) sheet into a seamless cylinder. Their utilization in advanced applications, such as structural materials in aerospace equipment and thermal management in electronics, depends on translating the superior properties of these building blocks, which are realized at the nanoscale along the long nanotube axis, into the final macroscopic materials. Therefore, achieving precise control over the orientation and packing of BNNTs within macroscopic assemblies is critical, as it directly enhances the mechanical strength and thermal efficiency of the materials, ensuring optimal performance in harsh environments. An effective method to fabricate aligned BNNT assemblies is through liquid processing of BNNT dispersions that exhibit a liquid crystalline (LC) phase.[8−14] The emergence of the LC phase promotes self-assembly, uniform alignment, and precise control over the orientation of individualized nanotubes. This approach simplifies the fabrication process, making it cost-effective and scalable for industrial applications. Moreover, BNNT LCs exhibit low light absorption, making them an intriguing model system for studying complex fluids composed of nanorods in regimes where CNT LCs have proven challenging to investigate (e.g., thick samples).[15]

Concentrated BNNT LCs have been obtained by dissolving highly crystalline BNNTs in chlorosulfonic acid (CSA).[8] Individualization of BNNTs in CSA through Coulombic repulsion is due to protonation of the nitrogen atoms of the outer BNNT wall, which leads to a positive net charge on the BNNT surface.[16] Simonsen Ginestra et al.[8] reported the formation of highly birefringent nematic domains of BNNTs in

Received: February 1, 2025
Revised: April 20, 2025
Accepted: April 23, 2025
Published: May 5, 2025

https://doi.org/10.1021/acs.langmuir.5c00563
Langmuir 2025, 41, 15270−15282

CSA at concentrations above 0.0170 wt %, indicating isotropic−nematic phase transition. The nematic alignment of high-purity BNNTs in CSA has also been observed via cryogenic electron microscopy.[17] Macroscopic assemblies, such as films and fibers of partially aligned BNNTs have been fabricated from BNNT−CSA solutions.[8,18] Although CSA effectively dissolves BNNTs without the need for compatibilizing agents, it is a strongly oxidizing acid that reacts with moisture to form gaseous HCl. Therefore, CSA poses difficulties of environmental control and material compatibility, particularly when working in a general laboratory environment. Moreover, LC formation in CSA requires highly purified BNNTs and brief sonication of samples, which may further limit the method applicability.[8] Hence, exploring alternative preparations that can be easily implemented in most laboratory settings is desirable for the broader study of BNNT fluids and their ensuing assemblies.

Aqueous dispersions of BNNTs using noncovalent functionalization routes, such as polymers,[19−21] biomolecules,[22−24] and surfactants[24−28] have been widely reported.[29] Yet, only a few studies have demonstrated the formation of LCs in such systems. Lim et al.[21] reported the formation of LCs of BNNTs dispersed in different polymeric stabilizers, including poly(vinylpyrrolidone), poly(4-vinylpyridine), and poly(vinylpyrrolidone-*r*-vinylimidazole). These LCs were prepared by concentrating dispersions through evaporation, achieving up to 22 wt % BNNT. These systems exhibited Schlieren textures under polarized light microscopy (PLM) and showed rheological behavior characteristic of LCs in shear rheometry. Fiber spinning of these BNNT LCs revealed that fiber properties strongly depend on the degree of BNNT alignment and type of stabilizer used. Given the difficulty of removing polymers from the final composites, identifying alternative dispersants that are easier to extract becomes crucial for most applications. Kode et al.[22] and Zhi et al.[30] fabricated films by concentrating BNNT−DNA dispersions through evaporation and filtration, respectively. Although the self-assembly of aligned BNNTs in these films suggests the formation of LC phase during the process, detailed investigations were not reported. Recently, Ko et al.[28] studied purification of BNNTs dispersed in sodium cholate (SC) via a polymer two-phase extraction. Concentrating the purified BNNTs in SC solution inside a sample cell by evaporation enabled BNNT alignment within birefringent nematic domains. Concentrating BNNT−SC dispersions via slow filtration has also led to the spontaneous alignment of BNNTs into polycrystalline domains.[31] While surfactants, such as SC, are easy to remove from the final macroscopic materials,[11] detailed examinations of the phase behavior of BNNT−surfactant systems, including the complex interplay between phase separation and phase transitions, remain unexplored.[32,33]

Here, we prepare highly concentrated, stable aqueous LC dispersions of BNNTs, up to 15 wt %, stabilized by sodium deoxycholate (SDC). Via PLM, we show that concentrated BNNT−SDC dispersions form large nematic LC domains. We study the effect of BNNT material purity and BNNT−SDC concentrations on the LC formation, construct the first phase diagram of BNNTs dispersed in surfactants, investigate the dispersion state with cryogenic electron microscopy (cryo-EM), and demonstrate the scalable processing of BNNT aqueous LC dispersions into aligned films.

EXPERIMENTAL SECTION

Preparation of Concentrated BNNT LC Dispersion. BNNTs were produced by BNNT, LLC (Newport News, VA) by the high-temperature−pressure method (HTP).[34] As-synthesized BNNTs were refined to remove residual elemental boron (we call this material lightly purified BNNTs: LP-BNNTs; product code: SP10-R). Further purification etches nanoscale nonnanotubular BN species, such as nanosheets, nanocages, and amorphous BN, creating highly purified BNNTs (HP-BNNTs; product code: high purity BNNT).[8,35] Concentrated LC dispersions of LP-BNNTs and HP-BNNTs were prepared by a two-step process: predispersion by speed-mixing and microscopic homogenization by sonication. Initially, 45 mg of BNNTs were added to 0.3 mL of SDC (≥98% BioXtra, purchased from Sigma-Aldrich) in water (1−10 wt % SDC) and mixed for 4 h with a FlackTek DAC 150 SpeedMixer at 3500 rpm, forming a viscous dispersion. Visually homogeneous dispersions were obtained using SDC solutions at concentrations of 4 wt % and above. At lower SDC concentrations, the dispersions consisted of visible large BNNT clusters. These dispersions were rendered homogeneous by the addition of SDC solution. Following predispersion, a few microliters of the dispersion were encapsulated in a rectangular glass capillary (VITROCOM, VitroTubes 5012-050, 0.1 mm × 1 mm × 50 mm) by flame and epoxy. The encapsulated dispersions were bath-sonicated (Branson, Series CPXH) at 40 kHz for ∼10 s to individualize the BNNTs and promote the formation of large LC domains. The BNNT concentrations for all samples were adjusted by diluting with the original surfactant solution to maintain a constant surfactant concentration. After each dilution, the samples were speed-mixed for 30 min prior to encapsulation in glass capillary and bath sonication.

For cryo-EM investigations and film fabrication, dispersions of HP-BNNTs in SDC were prepared by speed-mixing, followed by ultrasonication for 2 h. For each sample, ultrasonication was performed on the entire dispersion (0.3−1 mL) using Misonix sonicator 4000 equipped with a cup horn with a 14.0 cm inner diameter cup and a 6.4 cm horn diameter, operated at 20 kHz and 100% amplitude. The temperature of the cup was maintained at 15 °C during sonication using a cooling system.

Thermogravimetric Analysis. Thermogravimetric analyses (TGA) of BNNT puffballs and films were conducted using a Mettler Toledo TGA/DSC equipped with an autosampler. The samples were placed in 70 μL alumina crucibles. The temperature program consisted of an initial hold at 120 °C for 30 min under 100 mL/min flow of air to ensure moisture removal. Following this period, the temperature increased incrementally to 1200 °C at 10 °C per minute.

Light Microscopy. Polarized light microscopy (PLM) analyses were performed using a Zeiss Axioscope 5 microscope, equipped with a Zeiss Axiocam 208 camera and a 10 W white LED for transmitted light illumination. A $\lambda/4$, 6 × 20 compensator was utilized for the detailed phase transition studies. Image contrast for all PLM micrographs was uniformly adjusted across all samples using open-source ImageJ software. For the birefringence studies of films, transmitted light intensity was measured by averaging the pixel values throughout the visual field.

Electron Microscopy. Scanning electron microscopy (SEM) analysis of the dry material was performed using an FEI Helios NanoLab 660 SEM/FIB for BNNT purity assessment and an Apreo ChemiSEM system for film alignment assessment. For purity assessment, ∼0.1 mg of BNNTs were dispersed in 10 mL of 2-propanol (HPLC grade) via tip sonication for 2 min. 50 μL of the dispersions were placed on a silicon substrate and allowed to dry in air at room temperature. BNNT films were directly imaged on glass substrates without applying a conductive coating, at an accelerating voltage of 1 kV, and a working distance of about ∼3 mm, using the high-resolution in-the-column secondary electron detector.

High-resolution transmission electron microscopy (HR-TEM) was conducted using FEI Titan Themis^3 S/TEM at 300 kV. 50 μL of BNNTs dispersed in 2-propanol were drop-cast on lacey carbon grids and allowed to dry in air at room temperature.

https://doi.org/10.1021/acs.langmuir.5c00563
Langmuir 2025, 41, 15270−15282

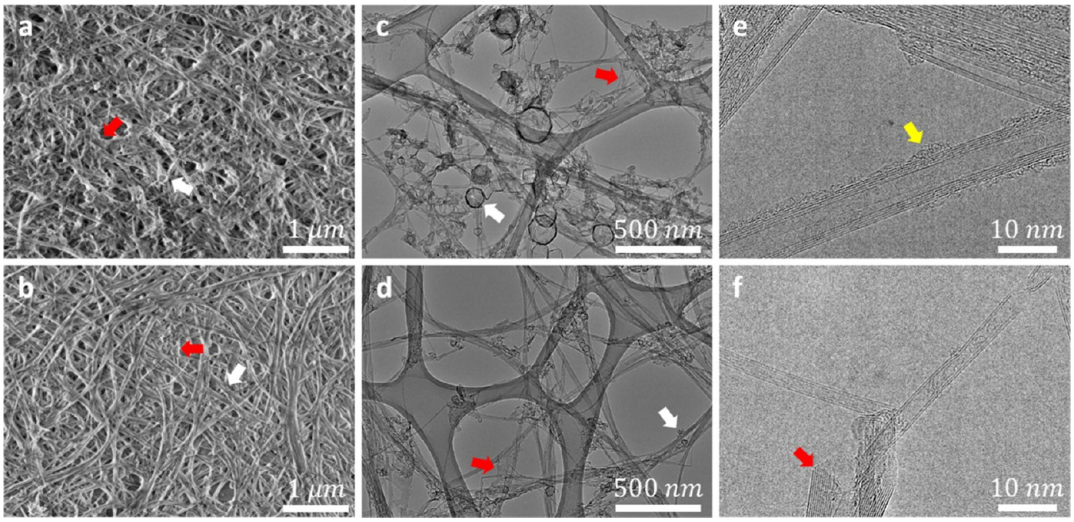

Figure 1. Electron microscopy of lightly purified BNNTs (LP-BNNTs) and highly purified BNNTs (HP-BNNTs). (a) Scanning electron microscopy (SEM) micrographs of LP-BNNTs showing a network of BNNT bundles together with large agglomerates of BN nanosheets (indicated by red arrows) and nanocages (indicated by white arrows). (b) SEM of HP-BNNTs displaying minimal h-BN presence compared to LP-BNNTs. (c) Transmission electron microscopy (TEM) of LP-BNNTs displaying high concentration and large BN nanocages. (d) TEM of HP-BNNTs with fewer and smaller nontubular nanostructures, indicating higher purity. Higher-resolution TEM of (e) LP-BNNTs and (f) HP-BNNTs, highlights clean surfaces of HP-BNNTs compared to LP-BNNT surfaces surrounded by amorphous BN (indicated by the yellow arrow).

Cryo-SEM was performed using a Zeiss Ultra Plus HR-SEM microscope, equipped with a field emission gun and a Leica VCT 500 cold-stage system. The specimen was maintained at −145 °C and imaged without a conductive coating. Low electron beam acceleration voltages (1 kV) and short working distances (up to 4 mm) were used to avoid specimen charging and imaging artifacts. Micrographs were taken with an in-the-column HR secondary electron detector. Cryo-SEM specimens were prepared in a controlled environment vitrification system (CEVS),[36] saturated with water vapor. The dispersion was applied on a TEM grid and excess material was blotted with a filter paper to obtain a thin layer of the sample. The specimen was plunged into liquid ethane and transferred into the microscope and maintained under cryogenic temperatures using a Leica EM VCM (vacuum cryo manipulation) system and EM VCT500 (vacuum cryo transfer) system.

Cryo-TEM was performed with an FEI (now Thermo Fisher Scientific) Talos 200C TEM, equipped with a field emission gun, and operated at 200 kV. Imaging was conducted in the low-dose mode of the TEM software, with image contrast enhanced using the Volta phase plate. Images were recorded by a Falcon III direct-imaging camera with the TIA software package. Cryo-TEM specimens were prepared in CEVS maintained at 25 °C, and saturated with water vapor. 3 μL of the dispersion was applied to a TEM copper grid with a supporting perforated carbon film. To form a thin film, excess material was blotted using a filter paper. The specimens were allowed to relax for 30 s to prevent artifacts from the blotting step. Specimens were vitrified by plunging into liquid ethane and then loaded into a Gatan 626 cryo-holder under liquid nitrogen. During imaging, the specimens were maintained in the TEM at −180 °C.

BNNT fiber cross-sectional lamella for TEM was prepared using an FEI Helios NanoLab 660 SEM/FIB. A 10 wt % HP-BNNT dispersion in 5 wt % SDC was loaded into a 1 mL syringe and injected into an ethanol bath, where it coagulated into a fiber. To protect the BNNTs from damage by the focused ion beam (FIB), a carbon layer of approximately 1 μm thick and 3 μm wide was deposited on the surface of the fiber. The fiber was then subjected to gallium ions from the FIB source to obtain a ∼3 μm thick cross-section. This cross-section was transferred on a half TEM grid and further thinned by FIB until the final lamella thickness reached ∼100 nm. TEM imaging was performed using an FEI Titan Themis[3] S/TEM operated at 300 kV.

Atomic Force Microscopy. Atomic force microscopy (AFM) was performed by a Nanoscope IIIa scanning probe microscope from Digital Instruments using a tapping mode. All micrographs were processed using the Gwyddion software package. Freshly cleaved mica was placed on a hot plate at ∼120 °C and primed with 20 mM $MgCl_2$. All BNNT dispersions were diluted to 0.01 wt % BNNT by the corresponding SDC solution. Diluted dispersions were transferred to a spray bottle and misted once over the mica surface. Excess surfactant was removed by dipping the mica into water, then soaking the mica in methanol for at least 1 min to remove any remaining surfactant. Immediately after washing, the samples were dried at 110 °C for at least 1 h before imaging. The thickness of the BNNT films was characterized using a Park AFM NX20 Microscope using a tapping mode after transferring the film to a mica disk and allowing it to dry in air.

X-ray Diffraction. X-ray diffraction (XRD) patterns were acquired using a Rigaku SmartLab II instrument. Experiments were conducted on BNNT films coagulated in chloroform and washed in IPA and water. Films were placed on clean glass slides, and dried in an oven for 2 h at 115 °C. HP-BNNTs were tested in their as-received form by compressing a "puffball" into a flat disk, which was then placed on a zero-background holder with a 5 mm × 0.2 mm well. The diffractions were collected over a 2θ range from 10 to 80° with a step size of 0.05° and scanning rate of 3°/min, using Cu Kα X-rays (wavelength λ = 1.54059 Å).

RESULTS AND DISCUSSION

BNNTs were produced by BNNT, LLC via the high-temperature−pressure method (HTP).[34] The synthesized BNNTs were purified by high-temperature steam treatment.[35] Here, refined BNNTs are referred to as lightly purified BNNTs (LP-BNNTs), while BNNTs that undergo further purification are referred to as highly purified BNNTs (HP-BNNTs). Thermogravimetric analysis (TGA) in air on both LP- and HP-BNNTs shows no mass gain below 900 °C, indicating the complete removal of residual elemental boron. Above 900 °C, the increase in mass is attributed to the oxidation of BN species (Figure S1).[35]

Scanning electron microscopy (SEM) and transmission electron microscopy (TEM) provide a qualitative comparison between the purity of LP- and HP-BNNTs. SEM of LP-BNNTs reveals a network of BNNT bundles, as shown in

https://doi.org/10.1021/acs.langmuir.5c00563
Langmuir 2025, 41, 15270−15282

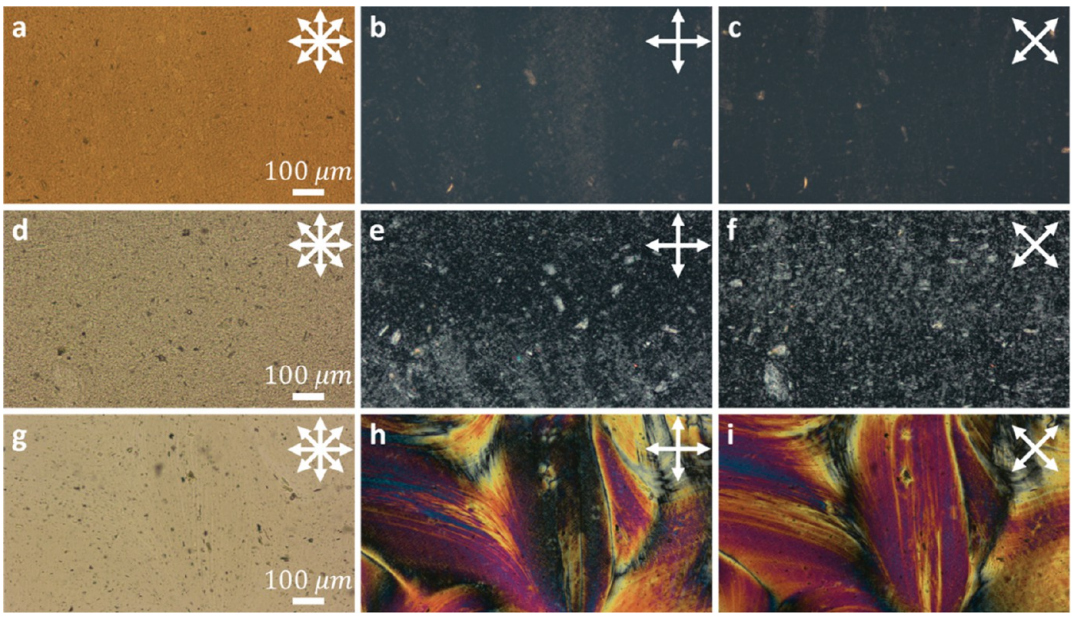

Figure 2. Transmitted polarized optical microscopy of 15 wt % LP- and HP-BNNT dispersions in 5 wt % SDC encapsulated in flame-sealed rectangular capillaries (1 mm × 0.1 mm). For the LP-BNNT dispersion: micrographs without polarizers (a) exhibit relatively strong light absorption, and with crossed polarizers at (b) 0°/90° and (c) 45°/135° display discontinuous, weak birefringent domains coexisting with isotropic regions that remain dark at all polarization angles. In contrast, micrographs of HP-BNNT dispersion without polarizers (d) demonstrate lower light absorption due to lower BN impurity content, and with crossed polarizers at (e) 0°/90° and (f) 45°/135° reveal small, bright birefringent domains. After sonicating the capillary of the HP-BNNT dispersion, micrographs without polarizers (g) present a more homogeneous dispersion, and with crossed polarizers at (h) 0°/90° and (i) 45°/135° reflect merging the smaller liquid crystalline domains into continuous ones spanning the entire capillary.

Figure 1a, coexisting with agglomerated BN nanosheets (indicated by red arrows) and nanocages (indicated by white arrows). SEM of HP-BNNTs in Figure 1b shows a network where the presence of BNNTs is remarkable, indicating successful removal of impurities. Low-magnification TEM images highlight the differences in size and concentration between the impurities remaining in LP-BNNTs compared to HP-BNNTs, as shown in Figure 1c,d, respectively. The nanocages in LP-BNNTs are significantly larger, up to ∼210 nm in diameter, while in HP-BNNTs, the largest nanocage observed was ∼62 nm in diameter. The nanocages in both samples appear hollow, indicating the removal of elemental boron, which is consistent with the TGA results. High-resolution TEM images reveal the surfaces of LP-BNNT to be partially wrapped by amorphous BN, as indicated by the yellow arrow in Figure 1e, in contrast to the cleaner surfaces observed in HP-BNNTs (Figure 1f).

The propensity to form liquid crystalline domains was studied for both LP- and HP-BNNTs. Highly concentrated dispersions of 15 wt % LP- and HP-BNNTs in 5 wt % SDC aqueous solutions were prepared directly by speed-mixing, avoiding more complex multistep processes reported in the literature.[9−11,21,37] The two dispersions were encapsulated in sealed glass capillaries and imaged via PLM. While slight differences can be appreciated between the dispersions in terms of translucency, both dispersions appeared macroscopically homogeneous (Figure S2); however microscopic examination by transmitted light without polarizers revealed that both dispersions contained aggregated BNNTs. BNNT aggregation, shown in Figure 2a,d, indicates incomplete BNNT dispersion due to insufficient energy provided by speed-mixing to overcome van der Waals attractions between bundled BNNTs, hindering efficient BNNT bundle exfoliation and surfactant coating. The LP-BNNT dispersion (Figure 2a) displays a stronger light absorption relative to the HP-BNNT dispersion (Figure 2d) stemming from the higher concentration of BN impurities in LP-BNNTs. Figure 2b,c show LP-BNNT dispersion between crossed polarizers at 0°/90° and 45°/135°, respectively, revealing weak birefringence with large regions that remain dark at all polarization angles. This implies low molecular ordering, prevented by nonnanotube BN impurities. However, the HP-BNNT dispersion between crossed polarizers (Figure 2e,f) displays bright birefringent regions, suggesting the formation of aligned domains of BNNTs. These domains appear small and coexist with isotropic regions, caused by the incomplete dispersion of BNNTs. Bath sonication of the capillary for ∼10 s promotes LC formation by merging the smaller liquid crystalline domains into continuous birefringent domains that span the whole capillary. This alignment is assisted by geometric confinement.[8] Under unpolarized transmitted light, the sonicated capillary of HP-BNNT dispersion exhibits a more homogeneous dispersion with fewer aggregates, as evidenced in Figure 2g. Figure 2h,i present crossed-polarized images of the fully nematic LC phase of BNNT−SDC dispersion.

Although Schlieren textures are typically observed in nematic LCs, our current system does not exhibit clear Schlieren textures. This is presumably due to perturbations caused by sonication. Even in unsonicated capillaries, the dispersion appears as small aggregates rather than defined textures. Previous studies of CNT dispersions have shown that smaller-diameter and shorter CNTs yield disturbed textures, while larger-diameter CNTs give rise to well-defined Schlieren textures.[10,38] The BNNTs used here ($D \sim 4.54$ nm, $L \sim 0.45$ μm) have a lower aspect ratio compared to previously reported BNNT−CSA LC solutions ($D \sim 5.6$ nm, $L \sim 1.54$ μm), which

https://doi.org/10.1021/acs.langmuir.5c00563
Langmuir 2025, 41, 15270−15282

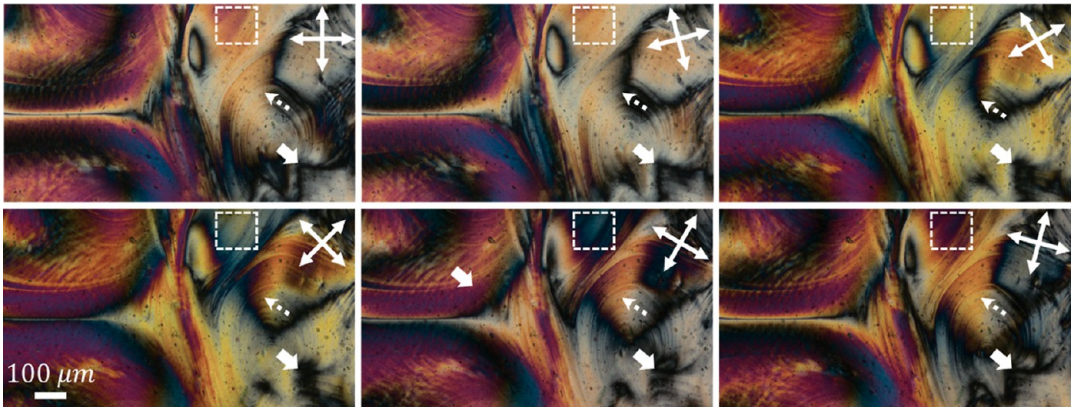

Figure 3. A series of transmitted polarized optical microscopy images of 15 wt % HP-BNNT dispersion in 5 wt % SDC, captured at 15° increments of crossed polarizers rotation. The LC texture shows three nematic domains with different elastic distortions: disclination point with two brushes indicative of splay distortion (solid white arrow), smoothly arced bands indicative of bend distortion (dashed white arrow), and regions that do not fully extinct at all polarization angles, which may be due to a twist in the nematic director (dashed white box).

were reported to display Schlieren textures at ∼0.73 wt % BNNT concentration in unsonicated capillaries.[8] However, the higher BNNT concentration in our samples significantly increases dispersion viscosity, hindering uniform shear alignment during speed-mixing. This results in fragmented domains resembling aggregates. Indeed, at high BNNT concentrations in CSA (5 wt % HP-BNNTs), unsonicated capillaries similarly show fragmented domain textures consistent with our observations (Figure S3). At lower BNNT concentrations, both systems display textures resembling those reported by Simonsen Ginestra et al.,[8] which closely approximate Schlieren textures but remain disturbed (Figure S4).

The liquid crystalline texture of 15 wt % HP-BNNT in the 5 wt % SDC dispersion reveals a nematic phase with splay and bend distortions, and an indication of twist distortion. Figure 3 shows a series of PLM images acquired between crossed polarizers rotated by 15° increments with three highlighted characteristic domains (see Movie S1 in the Supporting Information for continuous rotation of polarizers). The region highlighted by the solid white arrow shows a disclination point with two dark brushes. The region between the dark brushes becomes progressively extinct as the polarizers are being rotated. Unlike Schlieren textures, in which dark brushes connect different defects,[39] this region shows a singular defect of splay distortion. Smoothly arced bands, highlighted by the dashed white arrow, along with two dark brushes sweeping over them in the direction of the polarizers' rotation, indicate a large bend distortion. Highlighted by the dashed white box is a region in which small areas are never fully extinct at any polarization angle, which may be due to nematic domains exhibiting twist distortions. In fact, in many regions exhibiting splay and bend distortions, localized domains persist without reaching complete extinction at any polarization angle (see Movies S2 and S3 in the Supporting Information). While twist distortions are not as common as splay or bend distortions in nanotube LC systems without surface anchoring,[40] geometric confinement and mechanical stresses, induced by sonication, may produce localized twist distortions that contribute to the overall complexity of the nematic director field.[41−43] Overall, the LC textures in capillary-confined and sonicated BNNT−SDC dispersions suggest that twist distortions are more energetically favorable than splay or bend distortions.

Bath-sonicated capillary of LP-BNNT dispersion reveals the formation of the LC phase (Figure S5). However, the birefringence is weak, compared to HP-BNNT dispersion, indicating that the presence of impurities hinders the formation of highly ordered LC domains. Collectively, these findings underscore the influence of sonication and BNNT purity on the quality and optical properties of the dispersions, similar to earlier findings for BNNT LCs in CSA.[8]

The arrangement of HP-BNNTs within the LC phase was further examined by cryogenic temperature-SEM (cryo-SEM). For this investigation, 1 mL of 15 wt % HP-BNNT dispersion in 5 wt % SDC contained in a glass vial was cup-horn sonicated, rather than capillary sonicated, to promote LC formation at a larger scale than previously discussed (see Figure S6). It is noteworthy to mention that BNNT−SDC LC dispersions did not show a significant phase separation microscopically after several weeks (Figure S7). The cryo-SEM micrograph, shown in Figure 4a, displays the alignment of HP-BNNTs with a lack of positional order, a characteristic of nematic liquid crystals. To inspect the internal structure of the BNNT LC, the vitrified specimen was subjected to a controlled etching process by increasing its temperature to −100 °C for 5 min and then cooling it back to −145 °C. This process permitted water from the specimen surface to sublime, revealing inner structural details. The small thickness of the specimen allowed etching without causing undesirable crystallization. Figure 4b reveals the inner layer of the BNNT LC domains showing local alignment with varying orientational directors between neighboring domains (see white arrows). Additionally, we observe that the LC domains are composed of SDC-coated BNNTs, while impurities and surfactant residuals are found between neighboring domains. We did not observe clear disclination points, at which BNNTs changed orientational order between domains. This explains the absence of Schlieren textures in the BNNT−SDC LC system compared to CNT−surfactant systems wherein LCs were prepared by filtration.[37,44] Figure 4c shows direct imaging evidence of BNNT alignment into a wide nematic LC. Investigating the arrangement of BNNTs in LC dispersions via PLM and cryo-SEM uncovers the potential of sonication for exfoliating BNNT bundles and promoting LC formation, which is critical for their processing into macroscopic assemblies.

https://doi.org/10.1021/acs.langmuir.5c00563
Langmuir 2025, 41, 15270−15282

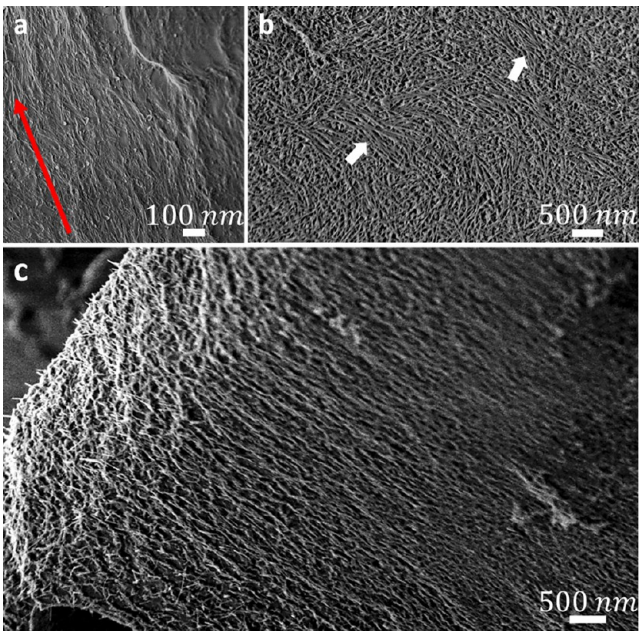

Figure 4. Cryogenic-SEM micrographs of 15 wt % HP-BNNT dispersion in 5 wt % SDC, captured (a) as prepared, and imaged at −145 °C. Despite the low contrast between the BNNTs and the surrounding water, a general directionality of the BNNTs, along the red arrow, is obtained. Exposing the inner structure of the BNNTs (b,c) after holding the specimen at −100 °C for 5 min, shows domains of nematic BNNT alignment with local alignment and varying orientation directors between neighboring domains [see white arrows in (b)], along with wider ordered nematic domains as shown in (c). Note the aligned domains are composed of pure SDC-coated BNNTs, while impurities/surfactant residuals separate between neighboring domains.

Determining the phase transition concentrations of BNNTs in surfactant systems is also essential for fabricating high-performance assemblies. Therefore, the 15 wt % HP-BNNT dispersion was diluted to study the phase transition while maintaining constant surfactant concentration at 5 wt %. The concentration of 5 wt % SDC was chosen for this study because BNNT dispersions that form liquid crystals required at least 5 wt % SDC, as will be discussed later in this paper. At 5 wt % BNNTs, the texture between crossed polarizers exhibits bright and dark regions, as shown in Figure 5a, which alternate in birefringence at different polarization angles (Figure S8). These observations suggest that the dispersion at 5 wt % BNNTs contains LC domains. The arrangement of BNNTs in this phase was investigated by placing a retardation plate at 45° to the polarizers, as indicated by the red arrow in Figure 5. A quarter wavelength retardation plate assists in determining the orientation of BNNTs in LC domains and enhances the contrast near isotropic cloud points by converting linearly polarized light into circularly polarized light. The right triangle of Figure 5a shows additive blue color and subtractive orange color, indicating the arrangement of BNNTs parallel and perpendicular to the optical axis of the retardation plate, respectively. At 2 wt % BNNTs, regions of optical anisotropy do not extend throughout the entire capillary, as observed in Figure 5b. Instead, they coexist with small dark regions that remain dark at all polarization angles (Figure S9). The right triangle of Figure 5b shows a purple color between the additive (blue) and subtractive (orange) domains which suggests that BNNTs situated between neighboring domains have a higher degree of deviation from their local alignment direction. This state is indicative of a biphasic system at the threshold of transitioning to fully nematic LC. At 1 wt % BNNTs, the isotropic phase dominates with very small birefringent domains, as shown in Figure 5c, indicated by white arrows (see Figure S10 for all polarization angles). The retardation plate enhances the contrast and allows the direct observation of localized birefringent nuclei or "swarms", as shown in the right triangle of Figure 5c. These swarms grow smaller or larger at lower or higher BNNT concentrations, respectively. Therefore, this condition suggests a biphasic state, nearing the isotropic cloud point. At an even lower concentration of 0.5 wt % BNNTs, shown in Figure 5d, the dispersion exhibits a uniform optical field, devoid of any birefringent textures, even with enhanced contrast, indicating the dispersion has reached the isotropic phase in which the BNNTs lack alignment (see Figure S11 for all polarization angles).

In the biphasic coexistence regime, spindle-shaped nematic tactoids of two morphologies, homogeneous and bipolar, were observed throughout all BNNT dispersions prior to sonication. Between crossed polarizers with a quarter wavelength retardation plate at 45° to the polarizers, homogeneous tactoids exhibited bright birefringence and extinction at ±45° (blue at +45°, orange at −45°) and 0°, respectively, indicating the arrangement of BNNTs along the long-axis of the tactoid (Figure 5e). Bipolar tactoids showed similar birefringence to the homogeneous tactoids at ±45° (Figure 5f). However, at 0° (or small tilt angles, ±10°), their lower-right and upper-left quadrants appeared blue, indicating BNNT alignment parallel to the optical axis of the retardation plate, while the opposing quadrants appeared orange, indicating perpendicular alignment to that axis. These observations align with the expected arrangement of BNNTs in bipolar tactoids and are consistent with the prior report of BNNT tactoid behavior in CSA solutions.[8] The average major axis lengths of homogeneous and bipolar tactoids in 1 wt % BNNT and 5 wt % SDC dispersion are 7.25 and 10.48 μm, respectively, which are smaller than those reported for BNNT bipolar tactoids in CSA (~20 μm).[8] Small tactoids exhibit a homogeneous director field, whereas larger tactoids show a bipolar director configuration, consistent with previous observations of CNT tactoids.[37,45] As tactoids grow, their shape transitions from elongated (average aspect ratio ~5.09) to spheroidal (average aspect ratio ~2.66) (Figure S12).

The experimental isotropic cloud point (where the isotropic−nematic separation occurs) and nematic cloud point (where the system transitions to fully nematic) were determined by averaging the concentrations at which the transitions were observed. Therefore, the experimental isotropic cloud point and nematic cloud point are 0.75 wt % (0.50 vol %) and 2.5 wt % (1.68 vol %), respectively. The conversion from wt % to vol % was performed using the following equation

$$\text{Vol \%}_{\text{BNNT}} = \frac{\text{wt \%}_{\text{BNNT}}}{\rho_{\text{BNNT}}\left(\frac{\text{wt \%}_{\text{BNNT}}}{\rho_{\text{BNNT}}} + \frac{100 - \text{wt \%}_{\text{BNNT}}}{\rho_{\text{solvent}}}\right)} \times 100 \quad (1)$$

where the density of BNNTs (ρ_{BNNT}) was averaged from values reported in literature,[46,47] resulting in an average of 1.5 g/mL, and the density of the solvent (ρ_{solvent}) was assumed to be the density of water.

https://doi.org/10.1021/acs.langmuir.5c00563
Langmuir 2025, 41, 15270−15282

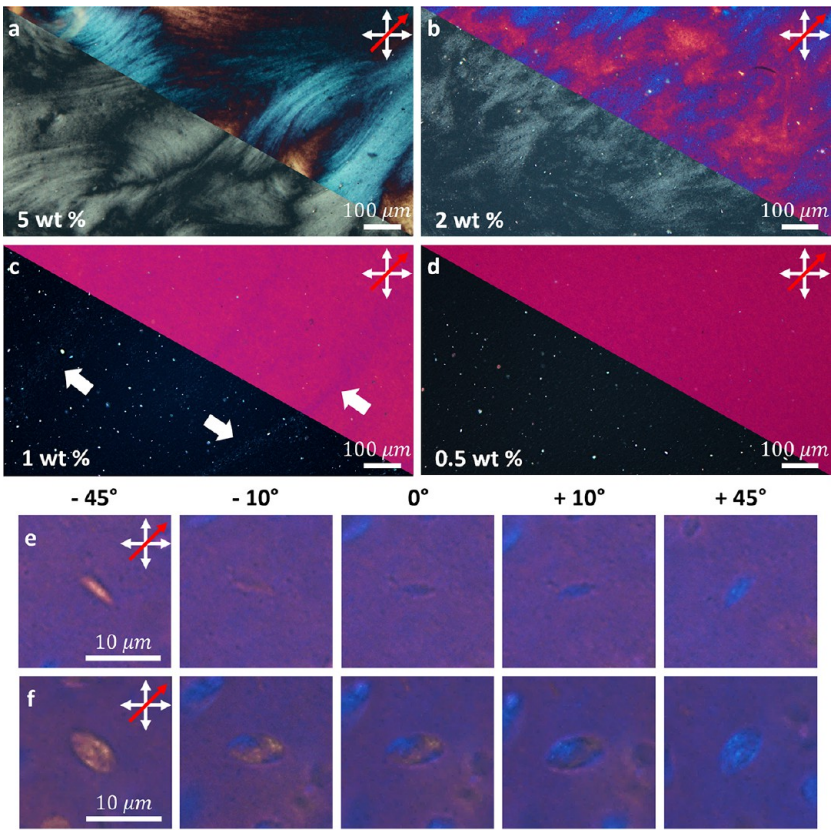

Figure 5. Phase transition of HP-BNNT in 5 wt % SDC dispersions between crossed polarizers with quarter wavelength retardation plate at 45° to the polarizer. (a) PLM images at 5 wt % HP-BNNT reveal a fully nematic liquid crystalline phase. (b) PLM images at 2 wt % HP-BNNT present large birefringent domains coexisting with small isotropic regions, indicating a biphasic state close to the nematic cloud point. (c) At 1 wt % HP-BNNT, the presence of locally ordered nuclei, or "swarms," (white arrows) suggests nearing the isotropic cloud point. (d) PLM images at 0.5 wt % HP-BNNT show an isotropic phase without any birefringent texture, which persists even under the retardation plate, confirming the absence of ordered structures. Note: Extra contrast was applied to (c,d) to enhance visibility. All bottom left triangles are PLM images obtained between crossed polarizers at 0°/90° without retardation plate. All upper-right triangles are PLM images captured between crossed polarizers at 0°/90° and a quarter wavelength retardation plate placed 45° to the polarizers (red arrow). Spindle-shaped BNNT tactoids in the biphasic coexisting state at 1 wt % HP-BNNT: (e) homogeneous tactoid exhibiting bright birefringence at ±45° and extinction at 0° and (f) bipolar tactoid showing similar birefringence at ±45° but quadrant-specific color changes at 0 and ±10° (blue where BNNTs align parallel to the retardation-plate axis; orange where they align perpendicular).

The Onsager theory is an effective tool for understanding the phase behavior of systems of rigid hard rods with length L and diameter D; it predicts the isotropic−nematic phase transition, with coexistence of the two phases over a concentration range.[48] The theory relies on the excluded volume interactions between rod-like molecules within a specified volume; the center of mass of two rods cannot occupy the same region. For an ideal solution of monodispersed, long, thin, and rigid rods, the phase boundaries are

$$\varphi_I = 3.34\left(\frac{D}{L}\right); \qquad \varphi_N = 4.49\left(\frac{D}{L}\right) \tag{2}$$

where, φ_I and φ_N are the volume fractions for the isotropic and nematic cloud points, respectively. Using atomic force microscopy (AFM), the average length and diameter of capillary sonicated HP-BNNT bundles in 5 wt % SDC were measured to be 452 ± 179 nm and 4.54 ± 2.02 nm, respectively (Figure S13). Based on Onsager's theory and the experimentally obtained aspect ratio (L/D = 116), the theoretical concentrations of φ_I and φ_N are 2.88 and 3.87 vol %, respectively. These values are much higher than the transition concentrations determined experimentally via PLM (φ_I = 0.5 vol % and φ_N = 1.68 vol %). It is known that polydispersity in rod length (or aspect ratio) causes the isotropic cloud point to occur at lower concentration (because the longer rods preferentially form liquid crystalline domains) and the nematic cloud point to occur at higher concentration (because shorter rods can remain isotropic at higher concentration), broadening the two-phase region.[49,50] Therefore, polydispersity may contribute to the observed early isotropic−biphasic phase transition but could not explain the lower nematic cloud point. We assume, based on cryo-TEM observations, that the earlier isotropic−biphasic and biphasic−nematic phase transitions could also be attributed to a possible incomplete BNNT dispersion and inefficient surfactant coating of individual BNNTs, resulting in unexfoliated BNNT bundles, as shown in Figure 6a. Those BNNT aggregates are of a size that is below the light microscopy resolution, hence, they cannot be seen at low concentrations via PLM. Higher-resolution cryo-TEM images reveal that BNNT bundles exhibit less dense packing (i.e., increased spacing between nanotubes within the bundles) with increasing surfactant concentration, as evident in Figure 6b,c compared to dispersions with 1 wt % SDC (Figure S14). This observation is presumably due to the increased efficiency of BNNT surfactant coating at the higher concentration of 5 wt % SDC. Moreover, these findings imply

https://doi.org/10.1021/acs.langmuir.5c00563
Langmuir 2025, 41, 15270−15282

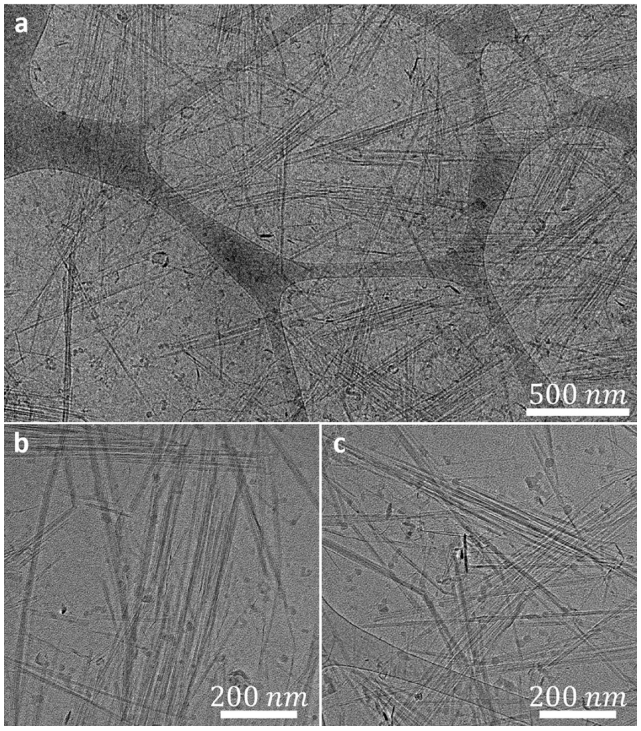

Figure 6. Cryo-TEM investigation of 0.1 wt % HP-BNNT dispersion in 5 wt % SDC. (a) Low magnification image showing multiple narrow BNNT aligned domains, with width below the resolution limit of light microscopy. (b,c) Higher magnification images of the typically observed aligned BNNT domains in the dispersion, showing less dense packing of the BNNTs within the bundles compared to BNNT dispersion with 1 wt % SDC. Those aligned BNNT bundles may promote the earlier development of the ordered nematic phase by serving as "nucleation sites". Note the black dots in the background of the SDC surfactant globular micelles.

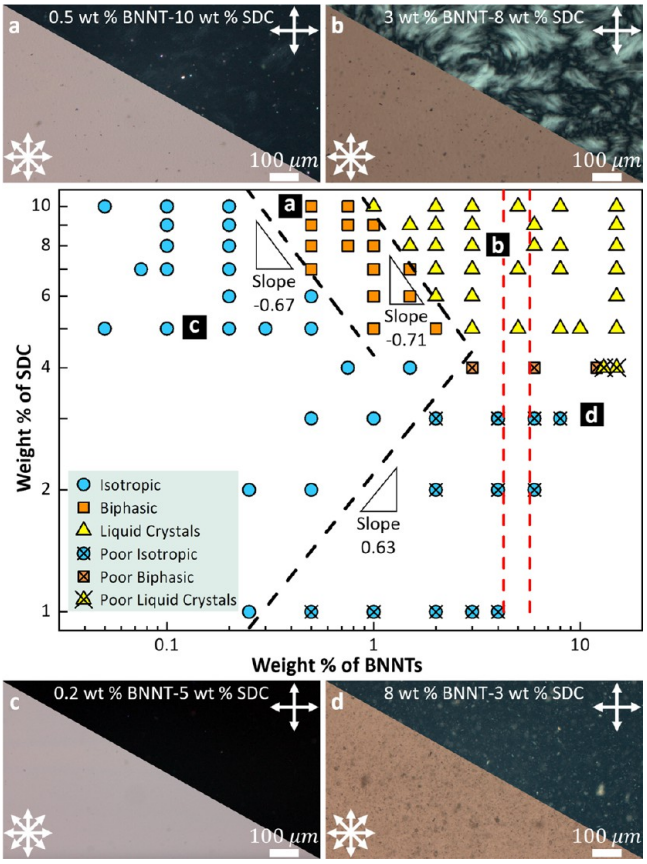

Figure 7. Phase Diagram of HP-BNNTs in aqueous solutions of SDC. The center panel shows the phase diagram which explains the various dispersion states of BNNTs in SDC as a function of their respective concentrations. The diagram is divided into distinct regions corresponding to different phases. The isotropic phase is represented by circles, indicating a homogeneous mixture without any alignment. The biphasic region, signified by squares, denotes the coexistence of isotropic and nematic phases. The region marked by triangles represents BNNT dispersions exhibiting a single LC phase. Crossed circles, squares, and triangles denote poor dispersions of BNNTs that exhibit isotropic, biphasic, and LC phases, respectively. Transmitted PLM images of BNNT dispersions in SDC at different mixture concentrations show the various dispersion phases. (a) Biphasic dispersion at 0.5 wt % BNNTs and 10 wt % SDC. (b) LC dispersion at 3 wt % BNNTs and 8 wt % SDC. (c) Isotropic dispersion at 0.2 wt % BNNTs and 5 wt % SDC. (d) Poor isotropic dispersion at 8 wt % BNNTs and 3 wt % SDC. All bottom-left triangles are obtained without polarizers. All upper-right triangles are captured between crossed polarizers at 0°/90°. Black dashed lines represent transition lines fitted using a scaled power law function ($y = ax^b$), with slope values indicated on the phase diagram. Vertical red dashed lines correspond to the theoretical transitions calculated for monodisperse BNNTs (aspect ratio, $L/D = 116$).

that the bundles may act as "nucleation sites", facilitating the incorporation of individual BNNTs or narrower bundles into an ordered nematic phase.

To further elucidate the early phase transition observations, it is worth extending the phase transition analysis to a range of different nanotube and surfactant concentrations, creating a phase diagram. The center panel of Figure 7 presents the first phase diagram of BNNT dispersions in surfactant, showing the effect of both BNNT and SDC concentrations on the phase transition. The phase diagram was constructed based on the identification of the three phases via PLM (see Figures S15 and S16 for phase diagram constructed with PLM micrographs). At BNNT concentrations above 2 wt % and SDC concentrations of 5 wt % and above, apparently homogeneous suspensions were obtained after speed-mixing for 4 h. Although aggregates were visible under the microscope in unsonicated capillaries, bath-sonicated capillaries displayed textures with smaller and fewer aggregates and long-range birefringent domains between crossed polarizers, as depicted in Figure 7b. As the BNNT concentration decreases below 2 wt %, the suspensions enter the biphasic regime, as shown in Figure 7a. Within this regime, the large birefringent domains gradually decrease in size as the suspension is diluted. Eventually, the appearance of swarms indicates that the suspension is nearing the concentration at which the transition to the isotropic phase occurs. The isotropic cloud point is determined when no birefringent texture is observed, similar to the dispersion in Figure 7c.

The effect of surfactant concentration on the phase transition is clearly seen in the center panel of Figure 7. As the SDC concentration increases, the isotropic cloud point shifts to a lower BNNT concentration, as depicted by the negative slope line between the isotropic and biphasic regions. For instance, the isotropic−biphasic transition occurs at approximately 0.75 and 0.35 wt % BNNTs for dispersions in 5 and 10 wt % SDC, respectively. This behavior contrasts with observations of CNTs dissolved in superacids. Increasing acid strength enhances the protonation of the nanotubes and further stabilizes the isotropic region (i.e., the isotropic cloud

https://doi.org/10.1021/acs.langmuir.5c00563
Langmuir 2025, 41, 15270−15282

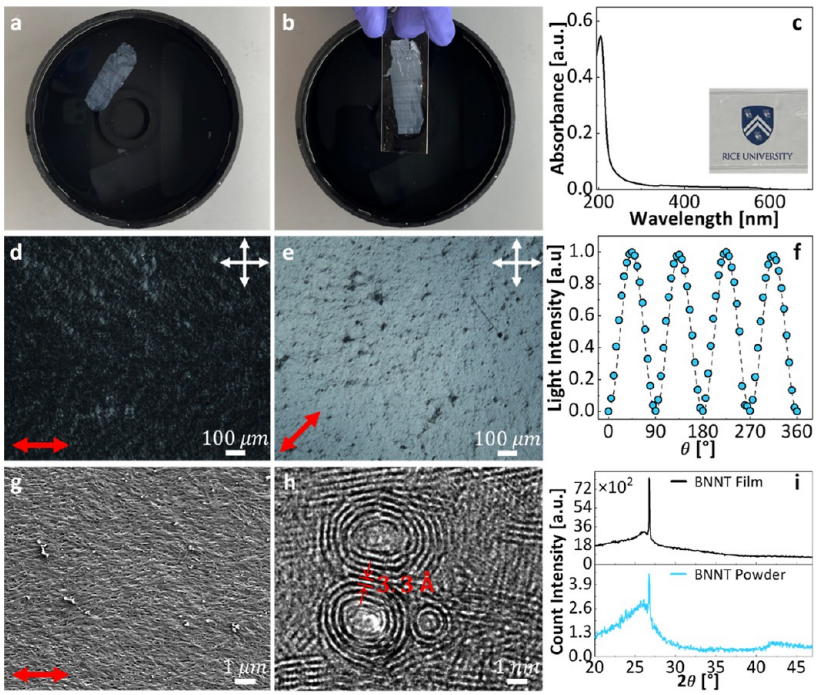

Figure 8. Aligned HP-BNNT film prepared by doctor blade method using 10 wt % HP-BNNT in 5 wt % SDC dispersion. (a) The BNNT film was floated on water after coagulation, demonstrating the film flexibility and ease of handling for transfer processes. (b) The BNNT film was transferred onto a quartz slide, showcasing its ability to be transferred onto various substrates after coagulation for different applications. (c) UV−vis spectrum of thin BNNT film, illustrating its high degree of transparency to visible light. The inset shows the BNNT film on top of the Rice University shield, further demonstrating its transparency. Transmitted PLM images of the BNNT film between crossed polarizers positioned at (d) 0°, displaying minimal birefringence, and (e) 45°, showing increased birefringence and confirming the alignment of BNNTs along the shearing direction (indicated by the double-headed red arrows). The dark spots in (e) are due to BNNT aggregation. (f) Normalized transmitted polarized light intensity through the BNNT film with respect to the stage rotation angle (blue circles) fitted to $\sin^2(\theta)\cos^2(\theta)$ (black dashed line). (g) SEM micrograph of the BNNT film showing aligned BNNT domains oriented along the shearing direction. (h) TEM micrograph of a cross-section of a BNNT bundle. (i) XRD pattern of BNNT film and as-received HP-BNNT showing a broad peak at 25.9° and a sharp peak at 26.8°. The high intensity of the sharp peak in the BNNT film, compared to the as-received HP-BNNT, suggests intertube contribution from well-aligned BNNT regions in the film.

point curve has a positive slope with increased acid strength).[51] This fundamental difference suggests that the complementary behavior arises from the distinct nature of the suspending agents, particularly the presence of micelles in surfactant-stabilized suspensions.

Depletion-induced attraction forces in surfactant-stabilized nanotube suspensions are well-documented in literature and widely recognized in colloidal science.[52] This phenomenon results from the exclusion of surfactant micelles in the gap between two nanotube bundles, creating an imbalance in the osmotic pressure that causes nanotube alignment and aggregation.[53] Surface tension measurements of SDC solution with and without nanotubes show that the critical micelle concentration (CMC) increases from 0.2 wt % SDC for solutions without BNNTs to 1 and 2 wt % SDC upon the inclusion of 0.1 and 0.5 wt % BNNT, respectively (Figure S17). Given the high SDC concentrations investigated in this work, we can predict that SDC micelles coexist with SDC-coated BNNTs in most of the dispersions presented in the isotropic region in the phase diagram (i.e., BNNT concentration ≤0.5 wt %). The coexistence of SDC micelles with SDC-coated BNNTs is further supported by the cryo-TEM results, as seen in Figure 6b,c. The globular micelles were observed in the dispersion of 0.05 wt % BNNTs and 1 wt % SDC as well (Figure S18). They are not observed in Figure S14 because the specimen was prepared too thin. Therefore, we attribute the negative slope of the isotropic cloud point curve to an increase in depletion-induced attraction force resulting from increased SDC concentration, a behavior also observed in sodium dodecyl sulfate[54]- and SC-stabilized[55] CNT suspensions.

Both depletion-induced alignment and polydispersity in rod length can explain the shift of the isotropic cloud point to lower BNNT concentrations; however, the mechanism underlying the decrease in the nematic cloud point with increasing surfactant concentration remains unclear. It is worth mentioning that SDC forms a hexagonal liquid crystalline phase above 20 wt % in water at room temperature,[56] though the SDC concentrations used in this study remain significantly lower (up to 10 wt %). While attractive van der Waals interactions between nanotubes have been proposed to explain the early nematic phase transition,[10,37,57] the precise mechanisms governing this behavior in the current system remain to be fully understood.

At 4 wt % SDC and high BNNT concentration, dispersions appeared more homogeneous than dispersions at lower SDC concentrations and displayed liquid crystalline domains coexisting with large undispersed clusters. At lower surfactant concentrations, poor dispersions that exhibited isotropic phase with visible aggregates were obtained. Large and dense clusters of BNNTs were still found even after capillary sonication, as shown in Figure 7d. The ratio of surfactant to nanotube concentrations is low to effectively disperse the BNNTs. Decreasing BNNT concentration increases this ratio, leading

https://doi.org/10.1021/acs.langmuir.5c00563
Langmuir 2025, 41, 15270−15282

to improved dispersion quality due to enhanced nanotube surface coating. Thus, the transitions observed at specific concentrations are critically dependent on the concentration of both BNNT and SDC. This phase diagram serves as a roadmap for preparing BNNT−SDC dispersions with the desired phase, which is essential for tailoring the processing and application of BNNT-based materials for optimal performance.

The potential for fabricating aligned thin macroscopic films from BNNT aqueous LC dispersions is demonstrated in Figure 8. Films were prepared by shearing 25 μL of 10 wt % HP-BNNT LC dispersion in 5 wt % SDC on top of a glass slide using the doctor blade method at a speed of ∼5 cm/s, followed by coagulation in chloroform. Figure 8a presents a coagulated film floating on the surface of a water bath, showcasing the successful detachment from the glass slide. Figure 8b shows the same film transferred onto a quartz slide, demonstrating the ease of transfer, which is important for various applications. The BNNT thin film is highly transparent to visible light, with noticeable absorption only in the UV region (at 204 nm), as illustrated by the UV−vis spectrum in Figure 8c and demonstrated by the inset, showing a transparent BNNT film on top of the Rice University shield.

We used PLM with crossed polarizers at 0°/90° to investigate the optical properties and alignment of the BNNT film. When the film is aligned with the polarizer at 0°, parallel to the shearing direction of the film, it exhibits minimal birefringence, as displayed in Figure 8d. Figure 8e shows that when the film is rotated 45° to the polarizer, it displays a significant increase in birefringence. This anisotropy in optical response is indicative of the orientation of BNNTs along the shearing direction. The dark spots in Figure 8e are due to BNNT aggregation. Figure 8f illustrates the normalized transmitted light intensity across various rotations of the BNNT film, modeled with a classical formula typical for anisotropic films: $\sin^2(\theta)\ \cos^2(\theta)$.[58] A strong correlation with this model suggests that the BNNT film is uniformly aligned along the shearing direction. We quantified the film alignment using the dichroic ratio, which measures the maximum to minimum transmitted light intensities, yielding an order parameter of $S = 0.52$.[59] The order parameter of this film, with a thickness of 249 ± 40 nm (Figure S19), is comparable to that reported for BNNT films fabricated from BNNT−CSA solutions.[8] Notably, this order parameter is higher than the values reported for CNT films of similar thickness.[10,60] This difference may arise from several factors, including nanotube concentration, dispersant, coagulant, and nanotube type.[60]

The alignment of BNNTs within the film was further investigated by SEM. Figure 8g shows an SEM micrograph of BNNT film coagulated in chloroform. The film consists of aligned BNNT domains oriented in the shearing direction, indicating the successful translation of BNNT alignment from the LC phase into macroscopic assemblies. We also explored other coagulation solvents to coagulate BNNT films including isopropanol, ethanol, and acetone. However, BNNT alignment in such films was much lower than the observed alignment in films coagulated in chloroform. Chloroform is a nonpolar solvent and insoluble in water which leads to a slower coagulation process allowing the BNNTs to maintain their LC phase alignment. Films that are allowed to dry in air for 5 min at room temperature before coagulation show improved alignment over films coagulated immediately after shearing (Figure S20).

A simple macroscopic method to evaluate the alignment of CNTs in films using X-ray diffraction (XRD) was proposed by Futaba et al.[61] that relates the intertube (spacing between nanotubes) contribution to the aggregation form of CNTs. We follow this method to further investigate the macroscopic alignment of BNNT films. The XRD pattern of the BNNT film shows a broad peak at 25.9° and a sharp, high-intensity peak at 26.8°, as shown in Figure 8i. The broad peak at 25.9° is due to the nanotube curvature and may suggest regions of randomly oriented BNNTs, while the sharp peak at 26.8°, typically associated with h-BN,[62,63] likely indicates contribution from well-aligned BNNT regions within the film.[61] TEM micrograph of a cross-section of BNNT bundle, presented in Figure 8h, shows the spacing between two adjacent nanotubes is approximately 3.3 Å, consistent with interlayer spacings of h-BN.[62] Therefore, the high intensity of the peak at 26.8° in the aligned BNNT film may be attributed to outer-shell contacts between BNNTs extending over long spans at nearly h-BN interlayer spacings. The XRD pattern in Figure 8i of as-received HP-BNNTs shows similar peaks positioned at the same diffraction angles. However, the relative intensity of the sharp peak to the broad peak is much lower in the as-received HP-BNNTs compared to the sheared film. The difference in the relative peak intensities, along with the cross-sectional TEM micrograph, supports the conclusion that the sharp peak at 26.8° results from intertube contributions in well-aligned BNNT regions, rather than from h-BN alone.

The thermal stability and composition of the BNNT films were probed by TGA. TGA of the BNNT film shows that the film is stable up to 800 °C in air (Figure S21). The residual surfactant content in the film after coagulation is approximately 3% by mass. This quantitative assessment is essential for understanding the composition of the film, informing the potential for posttreatment processes to completely remove the surfactant. Thus, we demonstrated the ability to fabricate and manipulate BNNT films with controlled alignment opening avenues for the development of advanced materials with tailored anisotropic properties, potentially impacting fields ranging from flexible electronics to composite materials.

CONCLUSION

In conclusion, we demonstrated the preparation of highly concentrated aqueous LC dispersions of HP-BNNTs stabilized by SDC. The results underscore the importance of BNNT purity in achieving long-range nematic LC domains. The arrangement of BNNTs within the nematic LC phase was directly visualized and confirmed using cryo-SEM. Detailed PLM studies led to the development of the first phase diagram for BNNTs in a surfactant system, describing the phase transitions from isotropic to biphasic and nematic phases as a function of BNNT and surfactant concentrations. This diagram serves as a roadmap for preparing BNNT dispersions with the desired phases and provides insights into the fundamental colloidal interactions within the system. Future investigations should aim to elucidate the mechanisms that govern the complex interactions between phase separation and phase transitions in BNNT−surfactant LC systems. The successful fabrication of well-aligned BNNT films from LC dispersions using scalable techniques demonstrates the applicability of this approach. The use of SDC not only enhances the alignment and dispersion quality of BNNTs but also aligns with the demand for safe processing methods. Overall, this study advances the understanding and application of BNNT liquid

https://doi.org/10.1021/acs.langmuir.5c00563
Langmuir 2025, 41, 15270−15282

crystals, contributing to the development of high-performance BNNT-based materials.

■ ASSOCIATED CONTENT

Supporting Information

The Supporting Information is available free of charge at https://pubs.acs.org/doi/10.1021/acs.langmuir.5c00563.

TGA of LP- and HP-BNNTs (Figure S1); macroscopic comparison of LP- and HP-BNNT dispersions in SDC (Figure S2); PLM images of high-concentration HP-BNNTs in CSA (Figure S3); PLM images of low-concentration HP-BNNTs in SDC and CSA (Figure S4); PLM images of capillary-sonicated LP-BNNT dispersion (Figure S5); PLM image of cup-horn sonicated BNNT−SDC dispersion (Figure S6); PLM images of cup-horn sonicated BNNT−SDC dispersion immediately after preparation and after 30 days (Figure S7); PLM images at different polarization angles of 5 wt % BNNT (Figure S8), 2 wt % BNNT (Figure S9), 1 wt % BNNT (Figure S10), and 0.5 wt % BNNT (Figure S11) dispersions in 5 wt % SDC; aspect ratio as a function of the major axis length of tactoids (Figure S12); length, height, and aspect ratio measurements of BNNT−SDC dispersions (Figure S13); cryo-TEM images of BNNT−SDC dispersions (Figure S14); phase diagram of BNNT−SDC dispersions via PLM (Figure S15); phase diagram of BNNT−SDC dispersions via PLM with $\lambda/4$ compensator (Figure S16); surface tension measurements of BNNT−SDC dispersions (Figure S17); cryo-TEM image of individualized BNNTs and SDC micelles (Figure S18); AFM measurement of a BNNT film (Figure S19); SEM micrographs of BNNT films (Figure S20); TGA of a BNNT film (Figure S21) (PDF)

Continuous crossed polarizers rotation of the region shown in Figure 3 (Movie S1) (MP4)

Continuous 360° sample rotation between crossed polarizers of the splay-twist (Movie S2) regions in capillary-sonicated dispersion of 15 wt % HP-BNNT in 5 wt % SDC (MP4)

Continuous 360° sample rotation between crossed polarizers of the bend-twist (Movie S3) regions in capillary-sonicated dispersion of 15 wt % HP-BNNT in 5 wt % SDC (MP4)

■ AUTHOR INFORMATION

Corresponding Author

Matteo Pasquali − *Department of Chemical and Biomolecular Engineering, Rice University, Houston, Texas 77005, United States; Department of Chemistry and The Smalley-Curl Institute, Rice University, Houston, Texas 77005, United States; Department of Materials Science and NanoEngineering, Houston, Texas 77005, United States;* orcid.org/0000-0001-5951-395X; Email: mp@rice.edu

Authors

Joe F. Khoury − *Department of Chemical and Biomolecular Engineering, Rice University, Houston, Texas 77005, United States;* orcid.org/0000-0002-6830-6562

Asia Matatyaho Ya'akobi − *Department of Chemical Engineering and The Russell Berrie Nanotechnology Institute (RBNI), Technion-Israel Institute of Technology, Haifa 3200003, Israel;* orcid.org/0000-0002-5342-8698

Alina Chow − *Department of Chemistry, Rice University, Houston, Texas 77005, United States*

Eldar Khabushev − *Department of Chemical and Biomolecular Engineering, Rice University, Houston, Texas 77005, United States*

Irina Davidovich − *Department of Chemical Engineering and The Russell Berrie Nanotechnology Institute (RBNI), Technion-Israel Institute of Technology, Haifa 3200003, Israel*

Davide Cavuto − *Department of Chemical and Biomolecular Engineering, Rice University, Houston, Texas 77005, United States*

Mingrui Gong − *Department of Chemical and Biomolecular Engineering, Rice University, Houston, Texas 77005, United States;* orcid.org/0009-0003-7245-188X

Lyndsey R. Scammell − *BNNT, LLC, Newport News, Virginia 23606, United States;* orcid.org/0000-0002-7133-7546

Cheol Park − *Advanced Materials and Processing Branch, NASA Langley Research Center, Hampton, Virginia 23681, United States*

Yeshayahu Talmon − *Department of Chemical Engineering and The Russell Berrie Nanotechnology Institute (RBNI), Technion-Israel Institute of Technology, Haifa 3200003, Israel;* orcid.org/0000-0002-9854-3972

Angel A. Martí − *Department of Chemical and Biomolecular Engineering, Rice University, Houston, Texas 77005, United States; Department of Chemistry and The Smalley-Curl Institute, Rice University, Houston, Texas 77005, United States; Department of BioEngineering, Houston, Texas 77005, United States; Department of Materials Science and NanoEngineering, Houston, Texas 77005, United States;* orcid.org/0000-0003-0837-9855

Complete contact information is available at: https://pubs.acs.org/10.1021/acs.langmuir.5c00563

Notes

The authors declare the following competing financial interest(s): Lyndsey R. Scammell is the Product Development Manager at BNNT, LLC, which has commercialized the synthesis of boron nitride nanotubes. The remaining authors declare no competing financial interest.

■ ACKNOWLEDGMENTS

We acknowledge the financial support of the Welch Foundation C-1668 and C-2152, NSF 2108838, NSF-BSF 2404270, and AFOSR FA9550-18-1-0014. We thank BNNT, LLC for providing the BNNTs used in this study. Cryo-TEM and HR-SEM imaging were performed at the Laboratory for Electron Microscopy of Soft Matter, supported by the Technion Russell Berrie Nanotechnology Institute (RBNI). We acknowledge the use of the Electron Microscopy Center (EMC) at Rice University and the Shared Equipment Authority at Rice University.

■ REFERENCES

(1) Blase, X.; Rubio, A.; Louie, S. G.; Cohen, M. L. Stability and Band Gap Constancy of Boron Nitride Nanotubes. *EPL* **1994**, *28*, 335−340.

(2) Lauret, J. S.; Arenal, R.; Ducastelle, F.; Loiseau, A.; Cau, M.; Attal-Tretout, B.; Rosencher, E.; Goux-Capes, L. Optical Transitions

in Single-Wall Boron Nitride Nanotubes. *Phys. Rev. Lett.* **2005**, *94*, 037405.
(3) Arenal, R.; Wang, M.-S.; Xu, Z.; Loiseau, A.; Golberg, D. Young Modulus, Mechanical and Electrical Properties of Isolated Individual and Bundled Single-Walled Boron Nitride Nanotubes. *Nanotechnology* **2011**, *22*, 265704.
(4) Chang, C. W.; Fennimore, A. M.; Afanasiev, A.; Okawa, D.; Ikuno, T.; Garcia, H.; Li, D.; Majumdar, A.; Zettl, A. Isotope Effect on the Thermal Conductivity of Boron Nitride Nanotubes. *Phys. Rev. Lett.* **2006**, *97*, 085901.
(5) Belkerk, B. E.; Achour, A.; Zhang, D.; Sahli, S.; Djouadi, M. A.; Yap, Y. K. Thermal Conductivity of Vertically Aligned Boron Nitride Nanotubes. *Appl. Phys. Express* **2016**, *9*, 075002.
(6) Chen, Y.; Zou, J.; Campbell, S. J.; Le Caer, G. Boron Nitride Nanotubes: Pronounced Resistance to Oxidation. *Appl. Phys. Lett.* **2004**, *84*, 2430−2432.
(7) Jakubinek, M. B.; Kim, K. S.; Kim, M. J.; Martí, A. A.; Pasquali, M. Recent Advances and Perspective on Boron Nitride Nanotubes: From Synthesis to Applications. *J. Mater. Res.* **2022**, *37*, 4403−4418.
(8) Simonsen Ginestra, C. J.; Martínez-Jiménez, C.; Matatyaho Ya'akobi, A.; Dewey, O. S.; Smith McWilliams, A. D.; Headrick, R. J.; Acapulco, J. A.; Scammell, L. R.; Smith, M. W.; Kosynkin, D. V.; Marincel, D. M.; Park, C.; Chu, S.-H.; Talmon, Y.; Martí, A. A.; Pasquali, M. Liquid Crystals of Neat Boron Nitride Nanotubes and Their Assembly into Ordered Macroscopic Materials. *Nat. Commun.* **2022**, *13*, 3136.
(9) Ao, G.; Nepal, D.; Aono, M.; Davis, V. A. Cholesteric and Nematic Liquid Crystalline Phase Behavior of Double-Stranded DNA Stabilized Single-Walled Carbon Nanotube Dispersions. *ACS Nano* **2011**, *5*, 1450−1458.
(10) Kojima, K.; Jintoku, H.; Kuwahara, Y.; Aizawa, M.; Yamamoto, T.; Muroga, S.; Kobashi, K.; Okazaki, T. Liquid-Crystalline Behaviors of Single-Walled Carbon Nanotube Aqueous Dispersions with Different Nanotube Aspect Ratios and Surfactants. *Appl. Phys. Express* **2022**, *15*, 125003.
(11) Maillaud, L.; Headrick, R. J.; Jamali, V.; Maillaud, J.; Tsentalovich, D. E.; Neri, W.; Bengio, E. A.; Mirri, F.; Kleinerman, O.; Talmon, Y.; Poulin, P.; Pasquali, M. Highly Concentrated Aqueous Dispersions of Carbon Nanotubes for Flexible and Conductive Fibers. *Ind. Eng. Chem. Res.* **2018**, *57*, 3554−3560.
(12) Mirri, F.; Ma, A. W. K.; Hsu, T. T.; Behabtu, N.; Eichmann, S. L.; Young, C. C.; Tsentalovich, D. E.; Pasquali, M. High-Performance Carbon Nanotube Transparent Conductive Films by Scalable Dip Coating. *ACS Nano* **2012**, *6*, 9737−9744.
(13) Mirri, F.; Orloff, N. D.; Forster, A. M.; Ashkar, R.; Headrick, R. J.; Bengio, E. A.; Long, C. J.; Choi, A.; Luo, Y.; Hight Walker, A. R.; Butler, P.; Migler, K. B.; Pasquali, M. Lightweight, Flexible, High-Performance Carbon Nanotube Cables Made by Scalable Flow Coating. *ACS Appl. Mater. Interfaces* **2016**, *8*, 4903−4910.
(14) Taylor, L. W.; Dewey, O. S.; Headrick, R. J.; Komatsu, N.; Peraca, N. M.; Wehmeyer, G.; Kono, J.; Pasquali, M. Improved Properties, Increased Production, and the Path to Broad Adoption of Carbon Nanotube Fibers. *Carbon* **2021**, *171*, 689−694.
(15) Jamali, V.; Mirri, F.; Biggers, E. G.; Pinnick, R. A.; Liberman, L.; Cohen, Y.; Talmon, Y.; Mackintosh, F. C.; Van Der Schoot, P.; Pasquali, M. Enhanced Ordering in Length-Polydisperse Carbon Nanotube Solutions at High Concentrations as Revealed by Small Angle X-Ray Scattering. *Soft Matter* **2021**, *17*, 5122−5130.
(16) Kleinerman, O.; Adnan, M.; Marincel, D. M.; Ma, A. W. K.; Bengio, E. A.; Park, C.; Chu, S.-H.; Pasquali, M.; Talmon, Y. Dissolution and Characterization of Boron Nitride Nanotubes in Superacid. *Langmuir* **2017**, *33*, 14340−14346.
(17) Matatyaho Ya'akobi, A.; Ginestra, C. J. S.; Scammell, L. R.; Smith, M. W.; Pasquali, M.; Talmon, Y. Electron Microscopy Study of BNNTs Synthesized by High Temperature−Pressure Method and Purified by High-Temperature Steam. *J. Mater. Res.* **2022**, *37*, 4508−4521.
(18) Adnan, M.; Marincel, D. M.; Kleinerman, O.; Chu, S. H.; Park, C.; Hocker, S. J. A.; Fay, C.; Arepalli, S.; Talmon, Y.; Pasquali, M. Extraction of Boron Nitride Nanotubes and Fabrication of Macroscopic Articles Using Chlorosulfonic Acid. *Nano Lett.* **2018**, *18*, 1615−1619.
(19) Jeon, S. W.; Kang, S. H.; Choi, J. C.; Kim, T. H. Dispersion of Boron Nitride Nanotubes by Pluronic Triblock Copolymer in Aqueous Solution. *Polymers* **2019**, *11*, 582.
(20) Maria Nithya, J. S.; Pandurangan, A. Aqueous Dispersion of Polymer Coated Boron Nitride Nanotubes and Their Antibacterial and Cytotoxicity Studies. *RSC Adv.* **2014**, *4*, 32031−32046.
(21) Lim, H.; Kim, Y.-K.; Kim, H.-S.; Lee, T.; Hossain, M. M.; Jeong, H.-O.; Lee, H. S.; Cho, H.; Joo, Y.; Lee, S. S.; Park, S.; Rho, H.; Jeong, H. S.; Kim, M. J.; Ahn, S.; Moon, S. Y.; Kim, K. S.; Choi, S. Q.; Kim, B. J.; Jang, S. G. Lyotropic Boron Nitride Nanotube Liquid Crystals: Preparation, Characterization, and Wet-Spinning for Fabrication of Composite Fiber. *ACS Appl. Mater. Interfaces* **2023**, *15*, 24681−24692.
(22) Kode, V. R.; Thompson, M. E.; McDonald, C.; Weicherding, J.; Dobrila, T. D.; Fodor, P. S.; Wirth, C. L.; Ao, G. Purification and Assembly of DNA-Stabilized Boron Nitride Nanotubes into Aligned Films. *ACS Appl. Nano Mater.* **2019**, *2*, 2099−2105.
(23) Kode, V. R.; Hinkle, K. R.; Ao, G. Interaction of DNA-Complexed Boron Nitride Nanotubes and Cosolvents Impacts Dispersion and Length Characteristics. *Langmuir* **2021**, *37*, 10934−10944.
(24) Khoury, J. F.; Vitale, J. C.; Larson, T. L.; Ao, G. Boron Nitride Nanotubes Enhance Mechanical Properties of Fibers from Nanotube/Polyvinyl Alcohol Dispersions. *Nanoscale Adv.* **2021**, *4*, 77−86.
(25) Smith McWilliams, A. D.; De Los Reyes, C. A.; Liberman, L.; Ergülen, S.; Talmon, Y.; Pasquali, M.; Martí, A. A. Surfactant-Assisted Individualization and Dispersion of Boron Nitride Nanotubes. *Nanoscale Adv.* **2019**, *1*, 1096−1103.
(26) Ko, J.; Kim, H. M.; Moon, S. Y.; Ahn, S.; Im, S. G.; Joo, Y. Highly Pure, Length-Sorted Boron Nitride Nanotubes by Gel Column Chromatography. *Chem. Mater.* **2021**, *33*, 4723−4732.
(27) Yu, J.; Chen, Y.; Cheng, B. M. Dispersion of Boron Nitride Nanotubes in Aqueous Solution with the Help of Ionic Surfactants. *Solid State Commun.* **2009**, *149*, 763−766.
(28) Ko, J.; Kim, D.; Sim, G.; Moon, S. Y.; Lee, S. S.; Jang, S. G.; Ahn, S.; Im, S. G.; Joo, Y. S. Scalable, Highly Pure, and Diameter-Sorted Boron Nitride Nanotube by Aqueous Polymer Two-Phase Extraction. *Small Methods* **2023**, *7*, 2201341.
(29) McWilliams, A. D. S.; Martínez-Jiménez, C.; Shumard, K. R.; Pasquali, M.; Martí, A. A. Dispersion and Individualization of Boron Nitride Nanotubes. *J. Mater. Res.* **2022**, *37*, 4459−4482.
(30) Zhi, C.; Bando, Y.; Wang, W.; Tang, C.; Kuwahara, H.; Golberg, D. DNA-Mediated Assembly of Boron Nitride Nanotubes. *Chem.—Asian J.* **2007**, *2*, 1581−1585.
(31) Kim, D.; Ko, J.; Kim, Y. K.; Lee, S. S.; Ahn, S.; Lee, S.; Jang, S. G.; Joo, Y. Spontaneous Alignment of Boron Nitride Nanotubes into Polycrystalline Film Arrays for Enhanced Piezoelectric Nanogeneration. *Small Struct.* **2024**, *5*, 2400259.
(32) Almohammadi, H.; Khadem, S. A.; Azzari, P.; Yuan, Y.; Guerra, A.; Rey, A. D.; Mezzenga, R. Liquid-Liquid Crystalline Phase Separation of Filamentous Colloids and Semiflexible Polymers: Experiments, Theory and Simulations. *Rep. Prog. Phys.* **2025**, *88*, 036601.
(33) Soule, E. R.; Rey, A. D. Modeling Complex Liquid Crystals Mixtures: From Polymer Dispersed Mesophase to Nematic Nanocolloids. *Mol. Simul.* **2012**, *38*, 735−750.
(34) Smith, M. W.; Jordan, K. C.; Park, C.; Kim, J. W.; Lillehei, P. T.; Crooks, R.; Harrison, J. S. Very Long Single-and Few-Walled Boron Nitride Nanotubes via the Pressurized Vapor/Condenser Method. *Nanotechnology* **2009**, *20*, 505604.
(35) Marincel, D. M.; Adnan, M.; Ma, J.; Bengio, E. A.; Trafford, M. A.; Kleinerman, O.; Kosynkin, D. V.; Chu, S. H.; Park, C.; Hocker, S. J. A.; Fay, C. C.; Arepalli, S.; Martí, A. A.; Talmon, Y.; Pasquali, M. Scalable Purification of Boron Nitride Nanotubes via Wet Thermal Etching. *Chem. Mater.* **2019**, *31*, 1520−1527.

https://doi.org/10.1021/acs.langmuir.5c00563
Langmuir 2025, 41, 15270−15282

(36) Bellare, J. R.; Davis, H. T.; Scriven, L. E.; Talmon, Y. Controlled Environment Vitrification System: An Improved Sample Preparation Technique. *J. Electron Microsc. Tech.* **1988**, *10*, 87−111.
(37) Kojima, K.; Aizawa, M.; Yamamoto, T.; Muroga, S.; Kobashi, K.; Okazaki, T. Liquid Crystalline Behaviors of Single-Walled Carbon Nanotubes in an Aqueous Sodium Cholate Dispersion. *Langmuir* **2022**, *38*, 8899−8905.
(38) Song, W.; Windle, A. H. Size-Dependence and Elasticity of Liquid-Crystalline Multiwalled Carbon Nanotubes. *Adv. Mater.* **2008**, *20*, 3149−3154.
(39) Dierking, I. *Textures of Liquid Crystals*; Wiley VCH: Weinheim, 2003.
(40) Chang, C.; Zhao, Y.; Liu, Y.; An, L. Liquid Crystallinity of Carbon Nanotubes. *RSC Adv.* **2018**, *8*, 15780−15795.
(41) Nayani, K.; Chang, R.; Fu, J.; Ellis, P. W.; Fernandez-Nieves, A.; Park, J. O.; Srinivasarao, M. Spontaneous Emergence of Chirality in Achiral Lyotropic Chromonic Liquid Crystals Confined to Cylinders. *Nat. Commun.* **2015**, *6*, 8067.
(42) Tortora, L.; Lavrentovich, O. D. Chiral Symmetry Breaking by Spatial Confinement in Tactoidal Droplets of Lyotropic Chromonic Liquid Crystals. *Proc. Natl. Acad. Sci. U.S.A.* **2011**, *108*, 5163−5168.
(43) Miller, D. S.; Carlton, R. J.; Mushenheim, P. C.; Abbott, N. L. Introduction to Optical Methods for Characterizing Liquid Crystals at Interfaces. *Langmuir* **2013**, *29*, 3154−3169.
(44) Song, W.; Windle, A. H. Isotropic-Nematic Phase Transition of Dispersions of Multiwall Carbon Nanotubes. *Macromolecules* **2005**, *38*, 6181−6188.
(45) Jamali, V.; Behabtu, N.; Senyuk, B.; Lee, J. A.; Smalyukh, I. I.; Van Der Schoot, P.; Pasquali, M. Experimental Realization of Crossover in Shape and Director Field of Nematic Tactoids. *Phys. Rev. E:Stat., Nonlinear, Soft Matter Phys.* **2015**, *91*, 042507.
(46) Mutz, M.; Eastwood, E.; Dadmun, M. D. Quantifying the Solubility of Boron Nitride Nanotubes and Sheets with Static Light Scattering and Refractometry. *J. Phys. Chem. C* **2013**, *117*, 13230−13238.
(47) Zhi, C.; Bando, Y.; Tang, C.; Golberg, D. Specific Heat Capacity and Density of Multi-Walled Boron Nitride Nanotubes by Chemical Vapor Deposition. *Solid State Commun.* **2011**, *151*, 183−186.
(48) Onsager, L. The Effects of Shape on The Interaction of Colloidal Particles. *Ann. N.Y. Acad. Sci.* **1949**, *51*, 627−659.
(49) Wensink, H. H.; Vroege, G. J. Isotropic-Nematic Phase Behavior of Length-Polydisperse Hard Rods. *J. Chem. Phys.* **2003**, *119*, 6868−6882.
(50) Tsentalovich, D. E.; Ma, A. W. K.; Lee, J. A.; Behabtu, N.; Bengio, E. A.; Choi, A.; Hao, J.; Luo, Y.; Headrick, R. J.; Green, M. J.; Talmon, Y.; Pasquali, M. Relationship of Extensional Viscosity and Liquid Crystalline Transition to Length Distribution in Carbon Nanotube Solutions. *Macromolecules* **2016**, *49*, 681−689.
(51) Davis, V. A.; Parra-Vasquez, A. N. G.; Green, M. J.; Rai, P. K.; Behabtu, N.; Prieto, V.; Booker, R. D.; Schmidt, J.; Kesselman, E.; Zhou, W.; Fan, H.; Adams, W. W.; Hauge, R. H.; Fischer, J. E.; Cohen, Y.; Talmon, Y.; Smalley, R. E.; Pasquali, M. True Solutions of Single-Walled Carbon Nanotubes for Assembly into Macroscopic Materials. *Nat. Nanotechnol.* **2009**, *4*, 830−834.
(52) Asakura, S.; Oosawa, F. On Interaction between Two Bodies Immersed in a Solution of Macromolecules. *J. Chem. Phys.* **1954**, *22*, 1255−1256.
(53) Bonard, J.-M.; Stora, T.; Salvetat, J.-P.; Maier, F.; Stockli, T.; Duschl, C.; Forró, L.; de Heer, W. A.; Châtelain, A. Purification and Size-Selection of Carbon Nanotubes. *Adv. Mater.* **1997**, *9*, 827−831.
(54) Vigolo, B.; Penicaud, A.; Coulon, C.; Sauder, C.; Pailler, R.; Journet, C.; Bernier, P.; Poulin, P. Macroscopic Fibers and Ribbons of Oriented Carbon Nanotubes. *Science* **2000**, *290*, 1331−1334.
(55) Im, J.; Jeong, Y. H.; Kim, M. C.; Oh, D.; Son, J.; Hyun, K.; Jeong, B.; Hong, S.; Lee, J. Wet Spinning of Multi-Walled Carbon Nanotube Fibers. *Carbon* **2024**, *216*, 118532.
(56) Su, Z.; Luthra, S.; Krzyzaniak, J. F.; Agra-Kooijman, D. M.; Kumar, S.; Byrn, S. R.; Shalaev, E. Y. Crystalline, Liquid Crystalline, and Isotropic Phases of Sodium Deoxycholate in Water. *J. Pharm. Sci.* **2011**, *100*, 4836−4844.
(57) Green, M. J.; Parra-Vasquez, A. N. G.; Behabtu, N.; Pasquali, M. Modeling the Phase Behavior of Polydisperse Rigid Rods with Attractive Interactions with Applications to Single-Walled Carbon Nanotubes in Superacids. *J. Chem. Phys.* **2009**, *131*, 084901.
(58) Zamora-Ledezma, C.; Blanc, C.; Maugey, M.; Zakri, C.; Poulin, P.; Anglaret, E. Anisotropic Thin Films of Single-Wall Carbon Nanotubes from Aligned Lyotropic Nematic Suspensions. *Nano Lett.* **2008**, *8*, 4103−4107.
(59) Chowdhury, R. A.; Peng, S. X.; Youngblood, J. Improved Order Parameter (Alignment) Determination in Cellulose Nanocrystal (CNC) Films by a Simple Optical Birefringence Method. *Cellulose* **2017**, *24*, 1957−1970.
(60) Jintoku, H.; Matsuzawa, Y. Carbon Nanotube Liquid Crystal Dispersion for Large-Area, Micropatterned Aligned Films. *ACS Appl. Nano Mater.* **2022**, *5*, 2195−2203.
(61) Futaba, D. N.; Yamada, T.; Kobashi, K.; Yumura, M.; Hata, K. Macroscopic Wall Number Analysis of Single-Walled, Double-Walled, and Few-Walled Carbon Nanotubes by X-Ray Diffraction. *J. Am. Chem. Soc.* **2011**, *133*, 5716−5719.
(62) Alkoy, S.; Toy, C.; Gdniil, T.; Tekin, A. Crystallization Behavior and Characterization of Turbostratic Boron Nitride. *J. Eur. Ceram. Soc.* **1997**, *17*, 1415−1422.
(63) Matović, B.; Luković, J.; Nikolić, M.; Babić, B.; Stanković, N.; Jokić, B.; Jelenković, B. Synthesis and Characterization of Nanocrystaline Hexagonal Boron Nitride Powders: XRD and Luminescence Properties. *Ceram. Int.* **2016**, *42*, 16655−16658.

https://doi.org/10.1021/acs.langmuir.5c00563
Langmuir 2025, 41, 15270−15282

Supporting Information

Lyotropic Liquid Crystalline Phase Behavior of Boron Nitride Nanotube Aqueous Dispersions

*Joe F. Khoury[1], Asia Matatyaho Ya'akobi[2], Alina Chow[3], Eldar Khabushev[1], Irina Davidovich[2], Davide Cavuto[1], Mingrui Gong[1], Lyndsey R. Scammell[4], Cheol Park[5], Yeshayahu Talmon[2], Angel A. Martí[1,3,6,7,8], and Matteo Pasquali[*1,3,7,8]*

[1] Department of Chemical and Biomolecular Engineering, Rice University, 6100 Main Street, MS 369, Houston, TX 77005, USA.

[2] Department of Chemical Engineering and The Russell Berrie Nanotechnology Institute (RBNI), Technion-Israel Institute of Technology, 3200003 Haifa, Israel.

[3] Department of Chemistry, Rice University, 6100 Main Street, MS 369, Houston, TX 77005, USA.

[4] BNNT, LLC, 300 Ed Wright Lane Suite A, Newport News, Virginia 23606, United States.

[5] Advanced Materials and Processing Branch, NASA Langley Research Center, Hampton, Virginia 23681, United States.

[6] Department of BioEngineering, 6100 Main Street, MS 369, Houston, TX 77005, USA.

[7] Department of Materials Science and NanoEngineering, 6100 Main Street, MS 369, Houston, TX 77005, USA.

[8] The Smalley-Curl Institute, Rice University, 6100 Main Street, MS 369, Houston, TX 77005, USA.

Corresponding Author

* mp@rice.edu

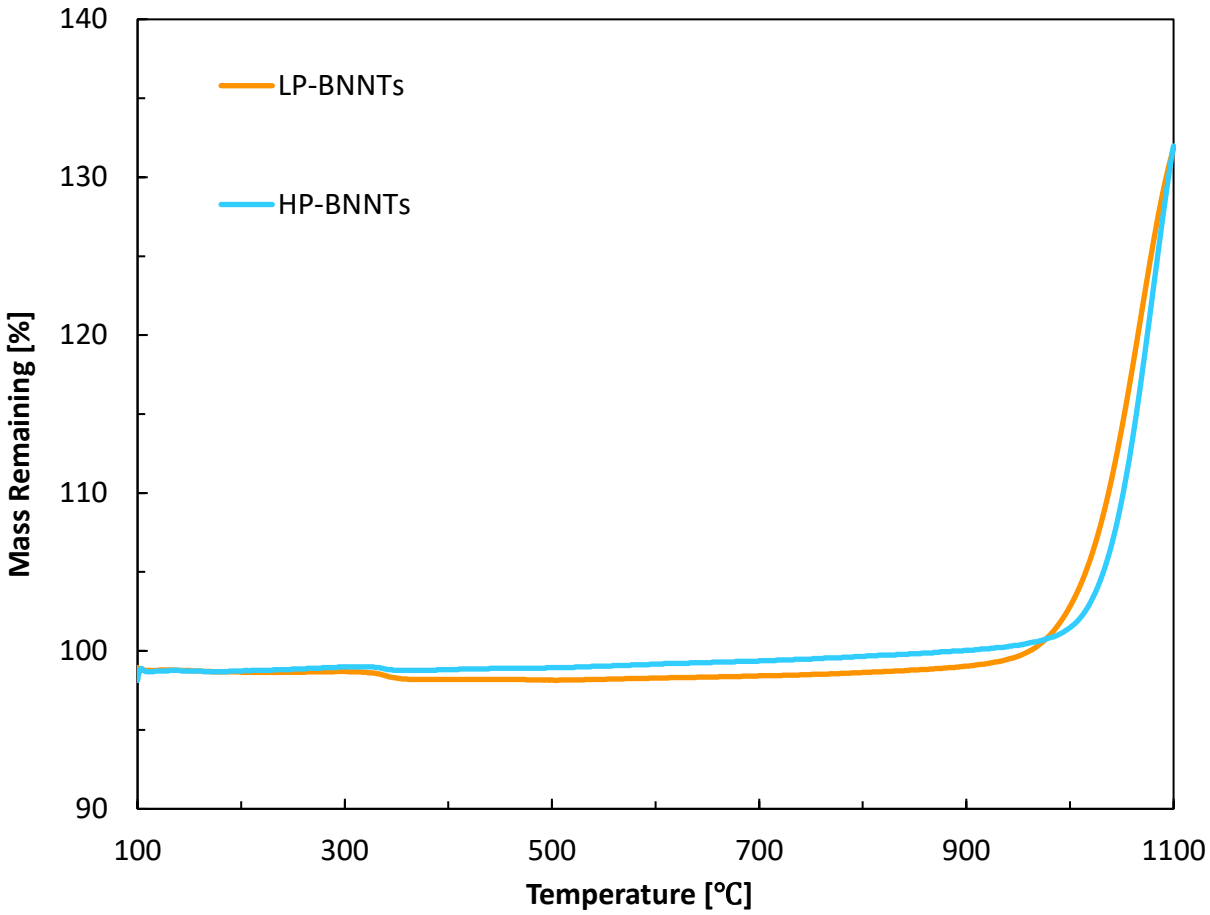

Figure S1. Thermogravimetric analysis (TGA). TGA was performed on LP- and HP-BNNTs over a temperature range from 100 °C to 1100 °C under an air atmosphere at a heating rate of 10 °C/min and an air flow of 100 mL/min.

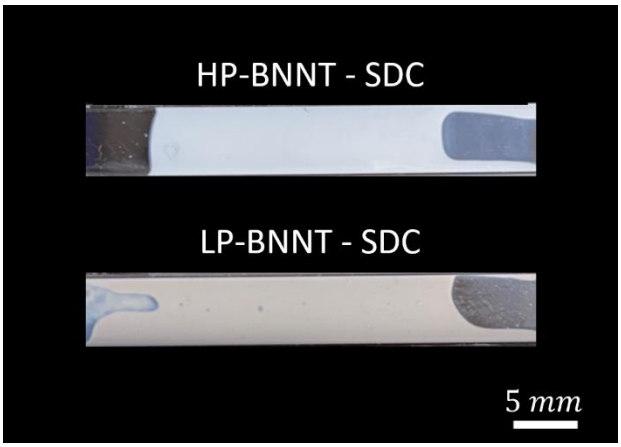

Figure S2. Visual comparison of dispersions of 15 wt % of LP- and HP-BNNTs in 5 wt % SDC. Both dispersions were speed mixed for 4 hours at 3500 RPM and loaded into rectangular capillaries

(0.5 mm x 5 mm). The HP-BNNTs dispersion appears white and translucent, while the LP-BNNTs dispersion is darker and less translucent in thin sections, indicating differences in dispersibility due to the purity of the BNNTs.

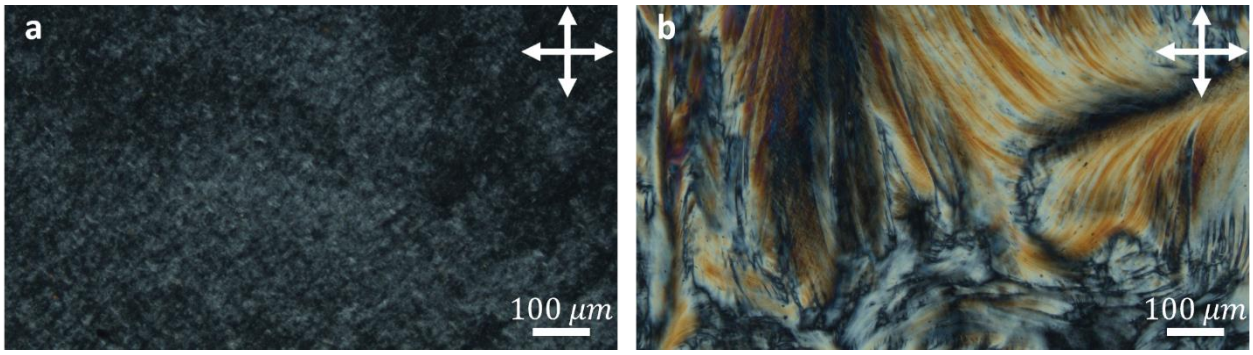

Figure S3. Transmitted polarizing light microscopy image of 5 wt % BNNTs in CSA encapsulated in a flame-sealed rectangular capillary (1 mm x 0.1 mm) after mixing the solution. Images were taken (a) before capillary sonication and (b) after capillary sonication.

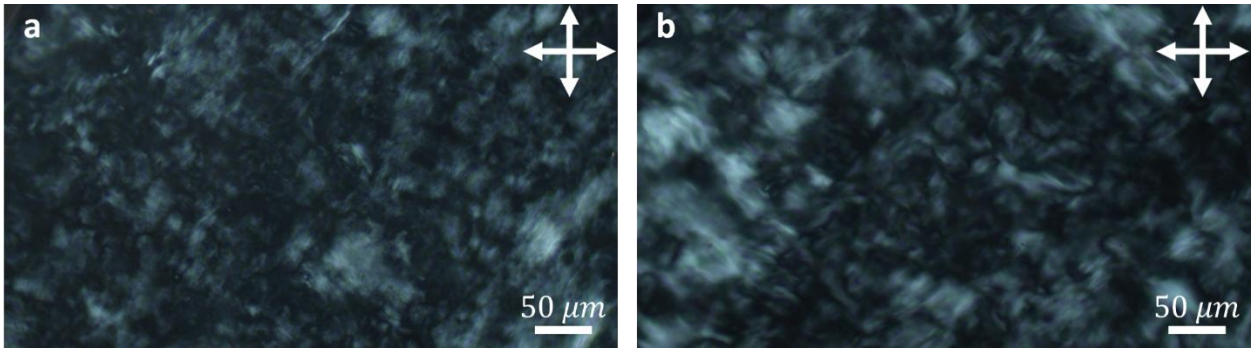

Figure S4. Transmitted polarizing light microscopy images of dispersions encapsulated in flame-sealed rectangular capillaries (1 mm × 0.1 mm) after mixing, without capillary sonication: (a) 1.5 wt % BNNTs in 5 wt % SDC and (b) 0.8 wt % BNNTs in CSA. Both systems display disturbed textures rather than well-defined Schlieren textures.

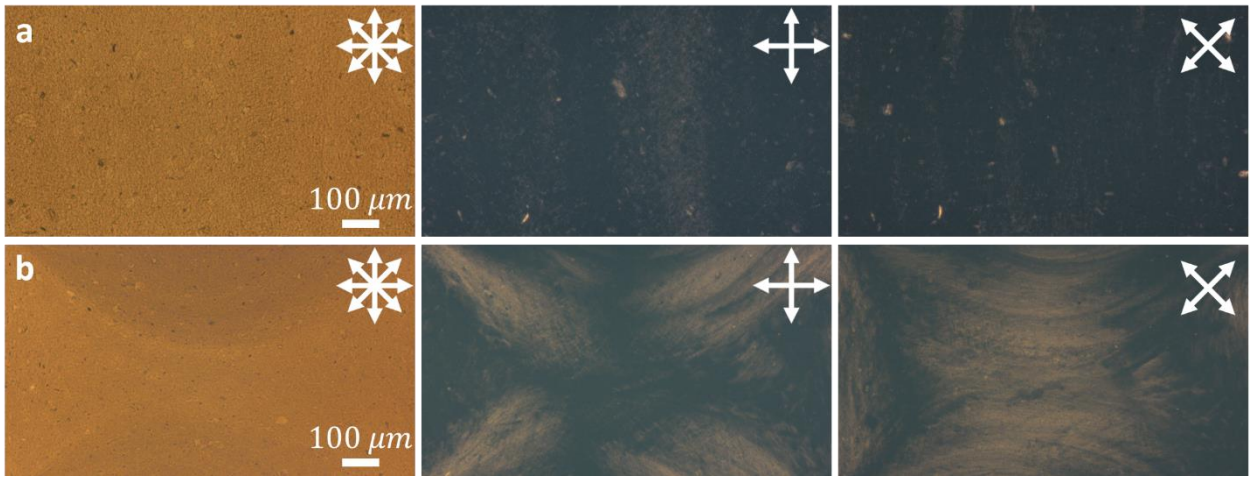

Figure S5. Transmitted polarizing light microscopy analysis of 15 wt % LP-BNNT dispersion in 5 wt % SDC encapsulated in flame-sealed rectangular capillaries (1 mm x 0.1 mm). (a) Sample before bath-sonication, displaying discontinuous and small birefringent regions with large aggregates. (b) Sample after bath-sonicating, showing the transformation of small birefringent domains into larger ones spanning the entire capillary with relatively weak birefringence due to the presence of impurities.

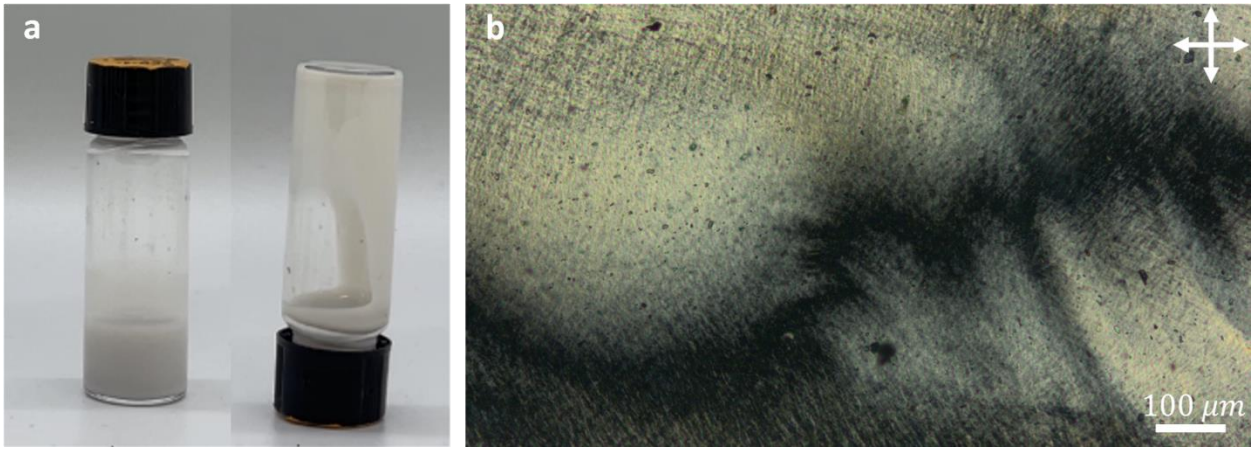

Figure S6. Cup-horn-sonicated vial of 15 wt % HP-BNNT dispersion in 5 wt % SDC. (a) The dispersion flows and does not behave like a gel after 1.5 hours of cup-horn sonication. (b) PLM image with crossed polarizers at 0°/90° of the dispersion encapsulated in a rectangular glass capillary.

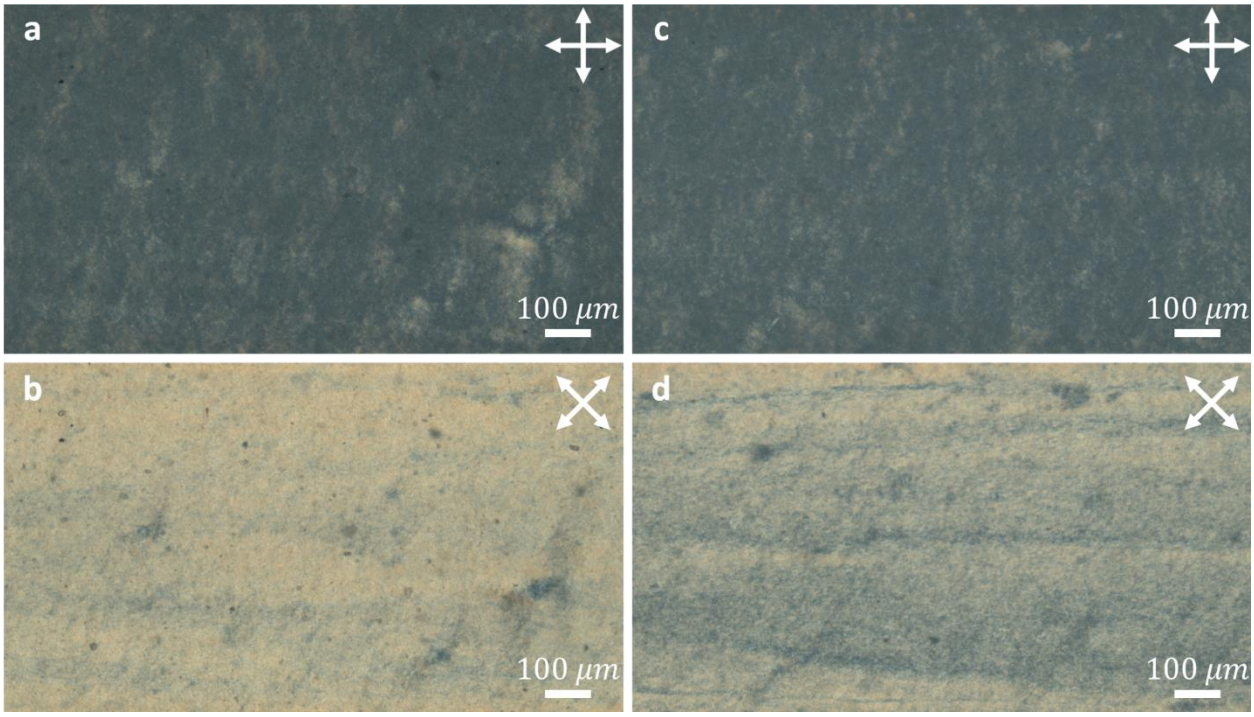

Figure S7. PLM images of an as-prepared 10 wt % HP-BNNT dispersion in 5 wt % SDC, encapsulated in a glass capillary after 2 hours of vial cup-horn sonication. Images (a) and (c) were taken at 0/90° and (b) and (d) at 45/135°. Panels (a) and (b) show the sample immediately after preparation, while (c) and (d) show the same capillary after 30 days, showing no significant phase separation.

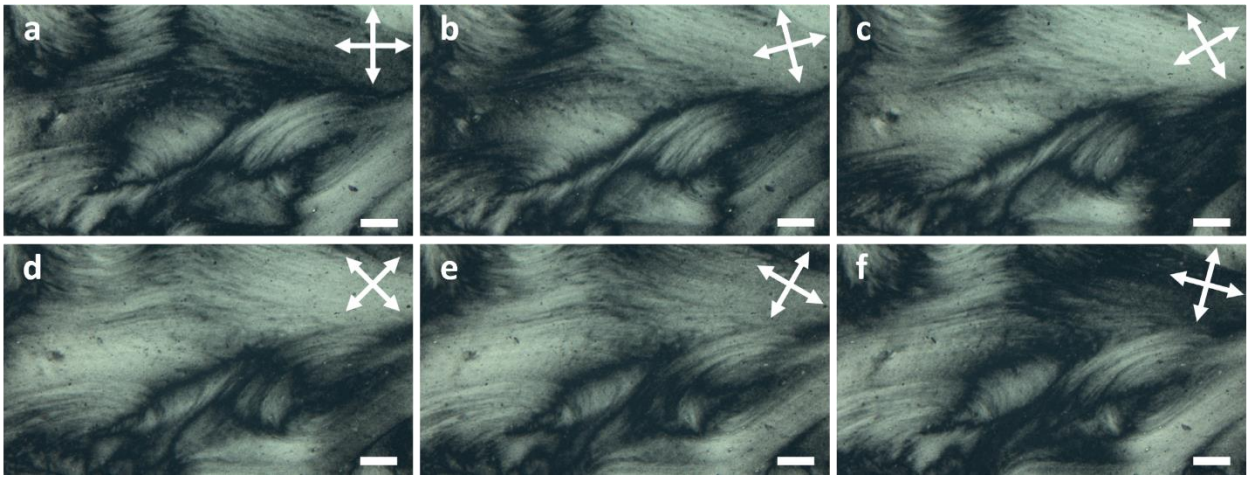

Figure S8. Series of PLM images of capillary bath sonicated 5 wt % HP-BNNT dispersion in 5 wt % SDC at different polarization angles. Crossed polarizers at (a) 0°/90, (b) 15°/105°, (c) 30°/120°, (d) 45°/135°, (e) 60°/150°, and (f) 75°/165°. Scale bars are 100 µm.

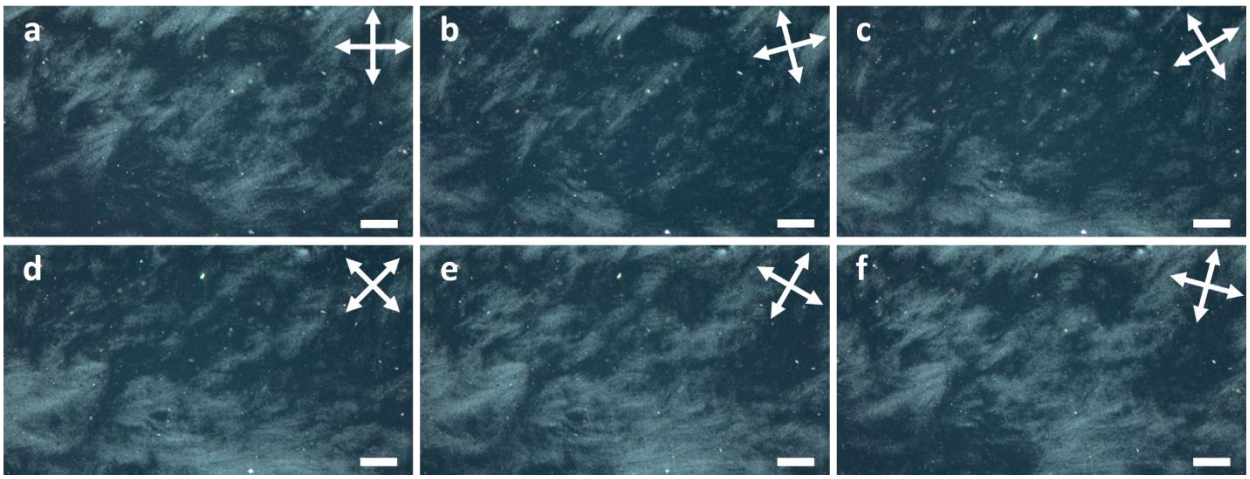

Figure S9. Series of PLM images of capillary bath sonicated 2 wt % HP-BNNT dispersion in 5 wt % SDC at different polarization angles. Crossed polarizers at (a) 0°/90, (b) 15°/105°, (c) 30°/120°, (d) 45°/135°, (e) 60°/150°, and (f) 75°/165°. Scale bars are 100 µm.

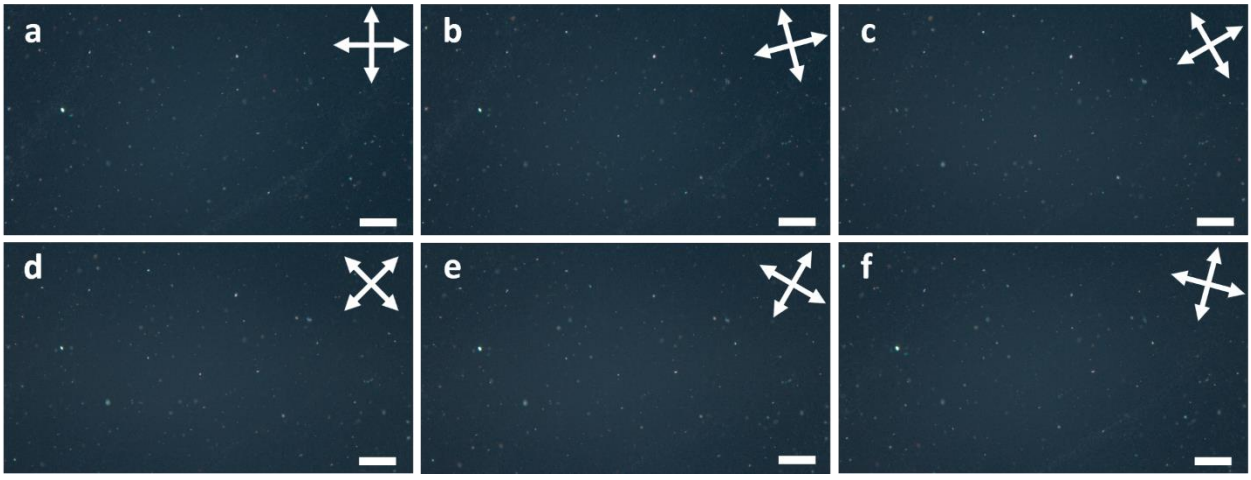

Figure S10. Series of PLM images of capillary bath sonicated 1 wt % HP-BNNT dispersion in 5 wt % SDC at different polarization angles. Crossed polarizers at (a) 0°/90, (b) 15°/105°, (c) 30°/120°, (d) 45°/135°, (e) 60°/150°, and (f) 75°/165°. Scale bars are 100 µm.

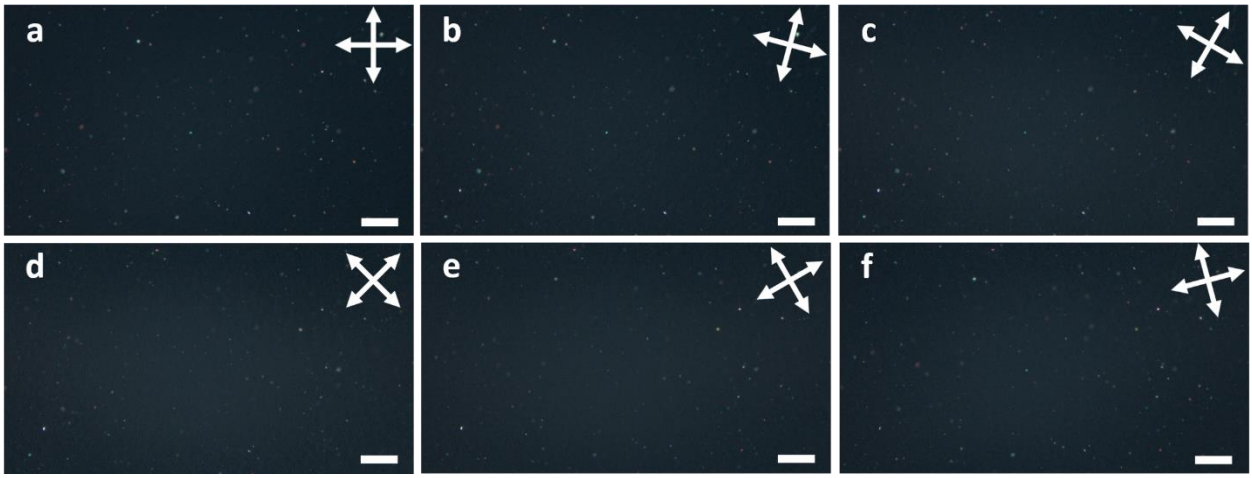

Figure S11. Series of PLM images of capillary bath sonicated 0.5 wt % HP-BNNT dispersion in 5 wt % SDC at different polarization angles. Crossed polarizers at (a) 0°/90, (b) 15°/105°, (c) 30°/120°, (d) 45°/135°, (e) 60°/150°, and (f) 75°/165°. Scale bars are 100 µm.

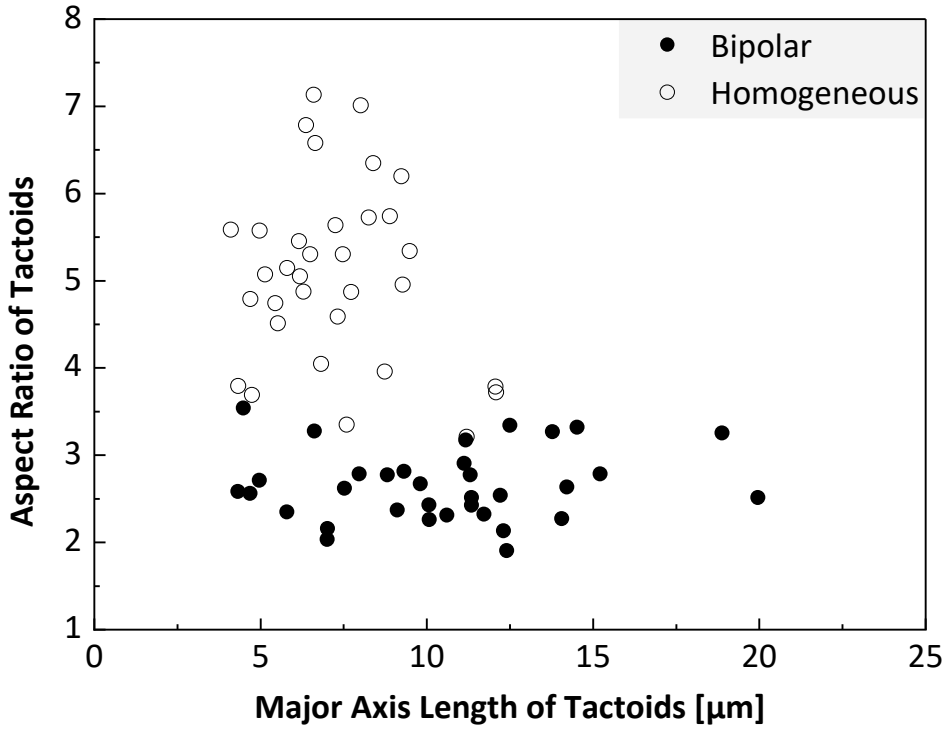

Figure S12. Aspect ratio as a function of the major axis length of 65 tactoids.

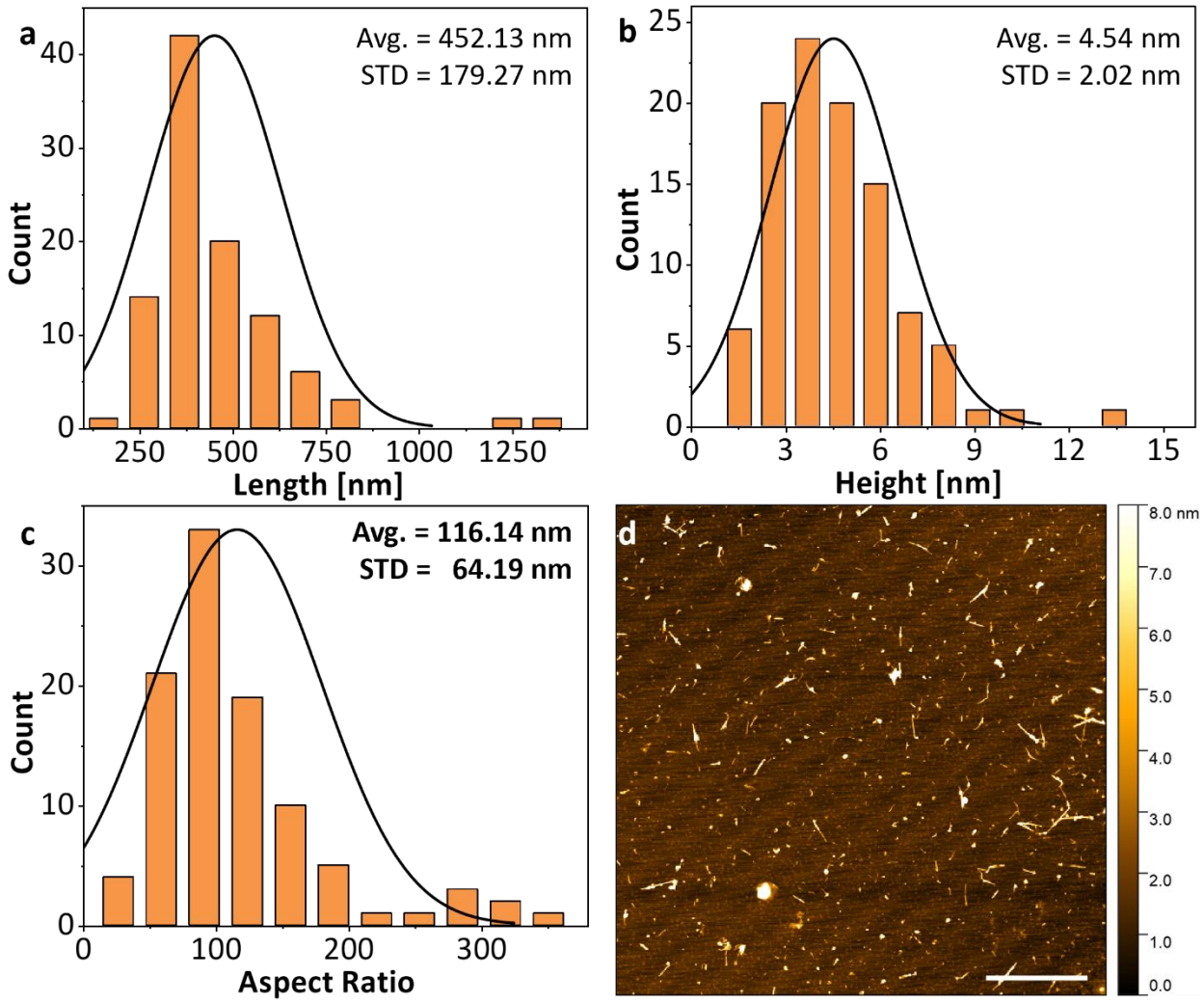

Figure S13. Histograms of (a) length, (b) height, and (c) aspect ratio distributions measured via AFM for bath-sonicated capillaries of HP-BNNT dispersions in 5 wt % SDC. Each histogram was fitted with a Gaussian curve to obtain an average (Avg.) distribution and standard deviation (STD). (d) AFM topographic image displaying the surface structure with nanoscale features. The scale bar represents 2 µm.

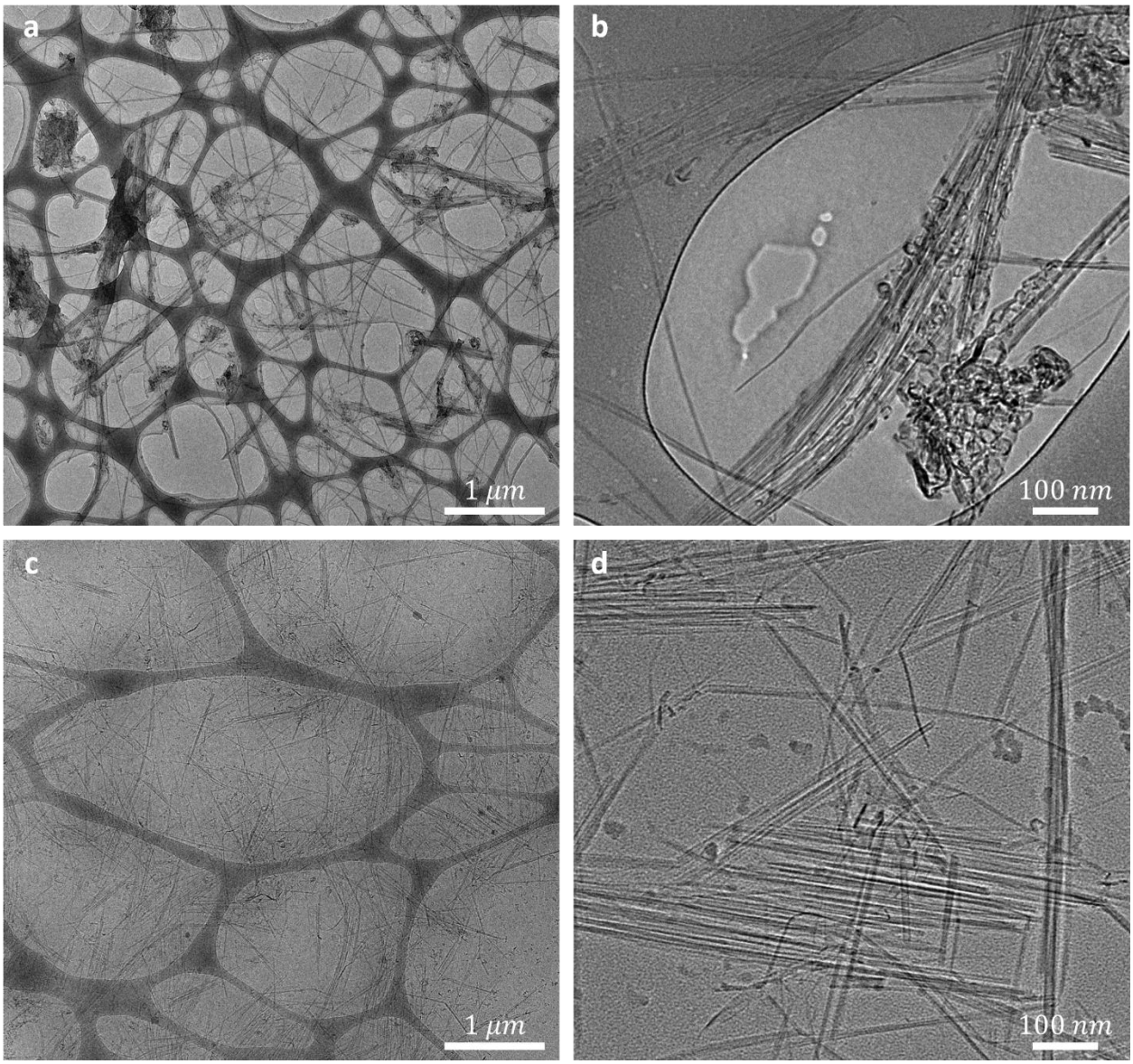

Figure S14. Cryo-TEM images of HP-BNNT dispersions in 1 wt % and 5 wt % SDC. (a) and (b) 0.05 wt % HP-BNNTs in 1 wt % SDC showing individually dispersed BNNTs along with unexfoliated, densely packed BNNT bundles. The absence of globular SDC micelles is due to the specimen being prepared too thin. (c) and (d) 0.1 wt % HP-BNNTs in 5 wt % SDC showing less dense packing of BNNTs, facilitating the incorporation of BNNTs into an ordered nematic phase.

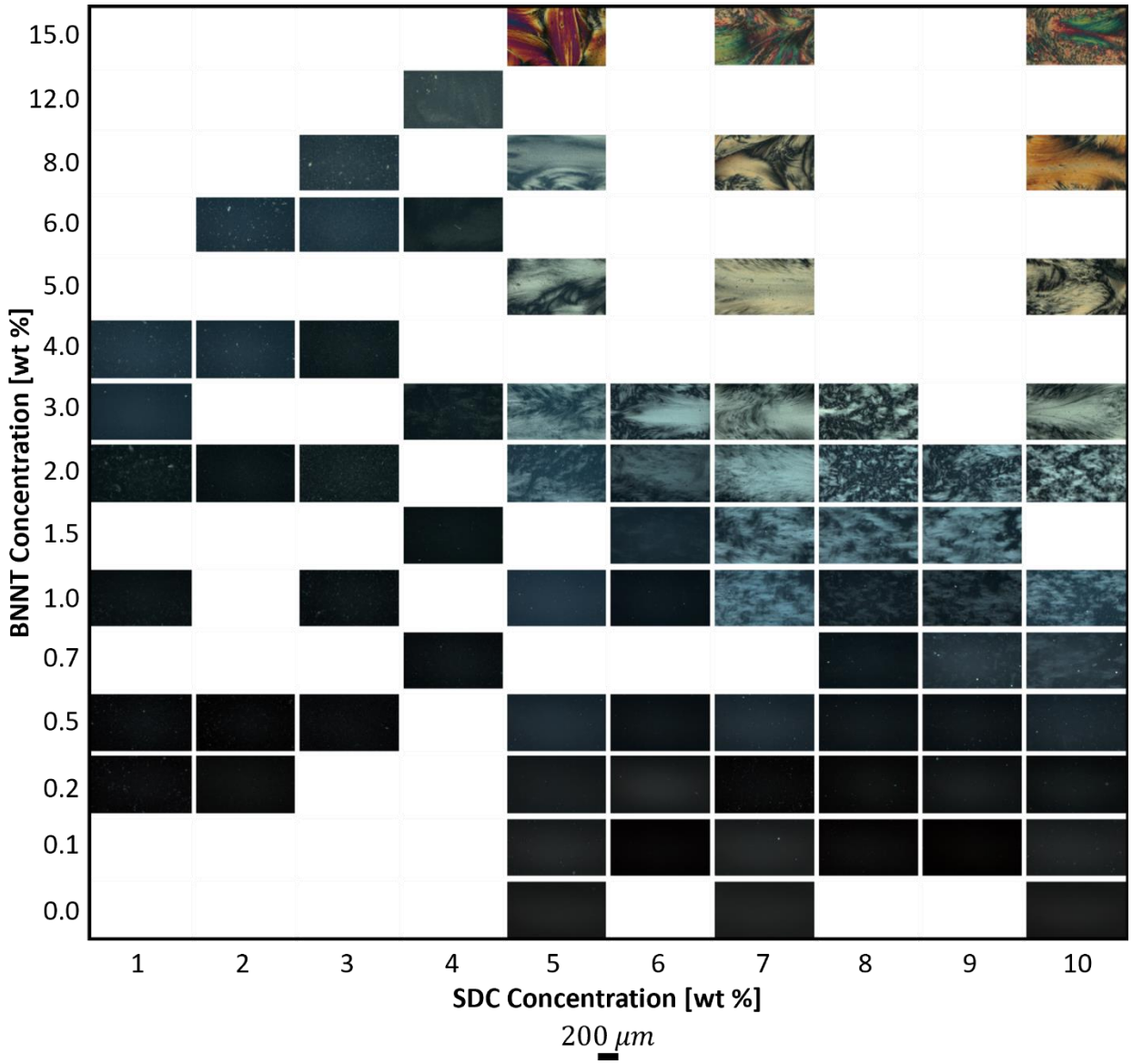

Figure S15. Phase diagram of HP-BNNT dispersions in SDC constructed of PLM micrographs. The phase diagram shows the various dispersion phases as a function of BNNT-SDC concentrations. All dispersions were encapsulated in rectangular capillaries (1 mm x 0.1 mm) and bath sonicated for ~10 seconds. PLM was performed between crossed polarizers at 0°/90°.

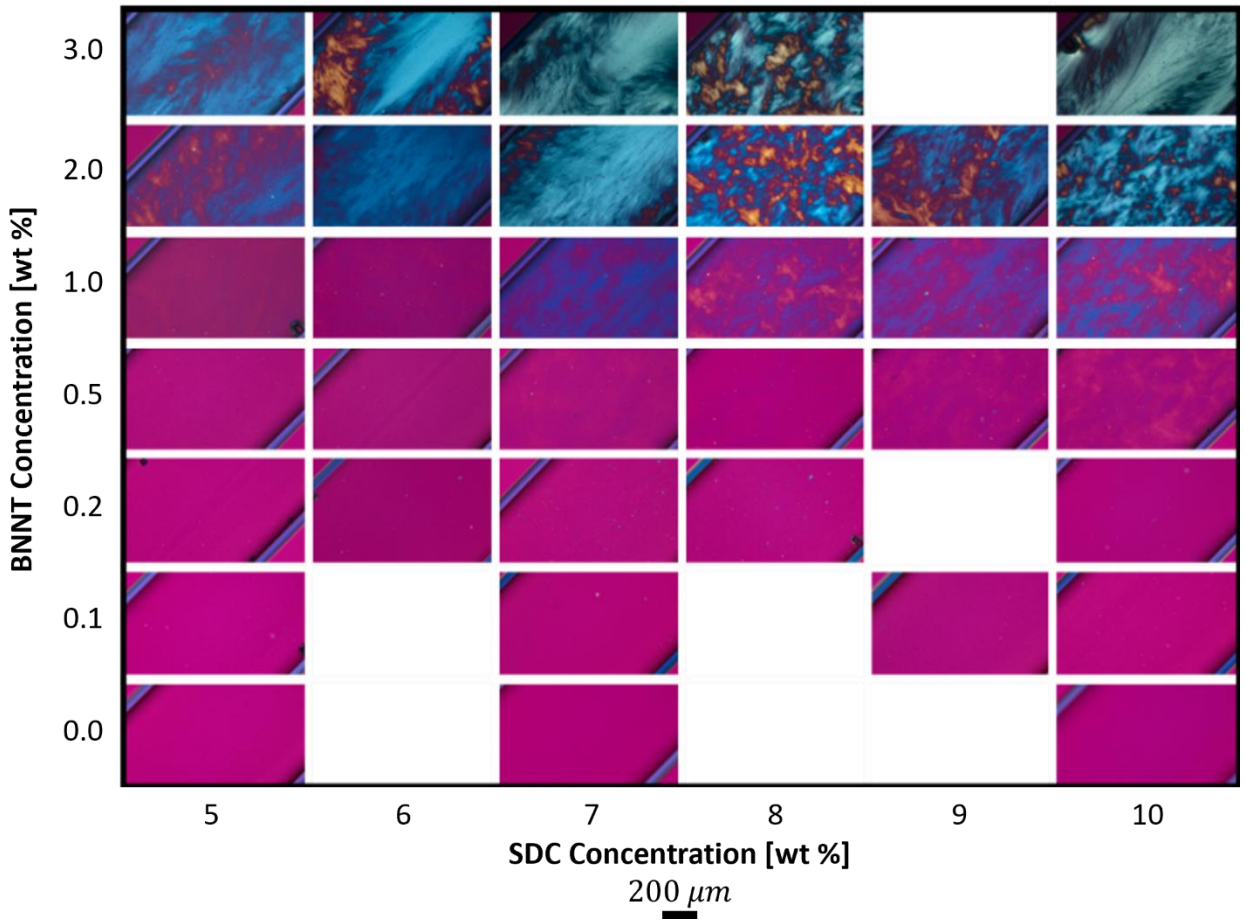

Figure S16. Phase diagram of HP-BNNT dispersions in SDC constructed of PLM micrographs with λ/4, 6x20 compensator inserted below the analyzer at 45° to the polarizer. The phase diagram shows the various dispersion phases as a function of BNNT-SDC concentrations. All dispersions were encapsulated in rectangular capillaries (1 mm x 0.1 mm) and bath sonicated for ~10 seconds. PLM was performed between crossed polarizers at 0°/90°, while capillaries were rotated 45° to the polarizer.

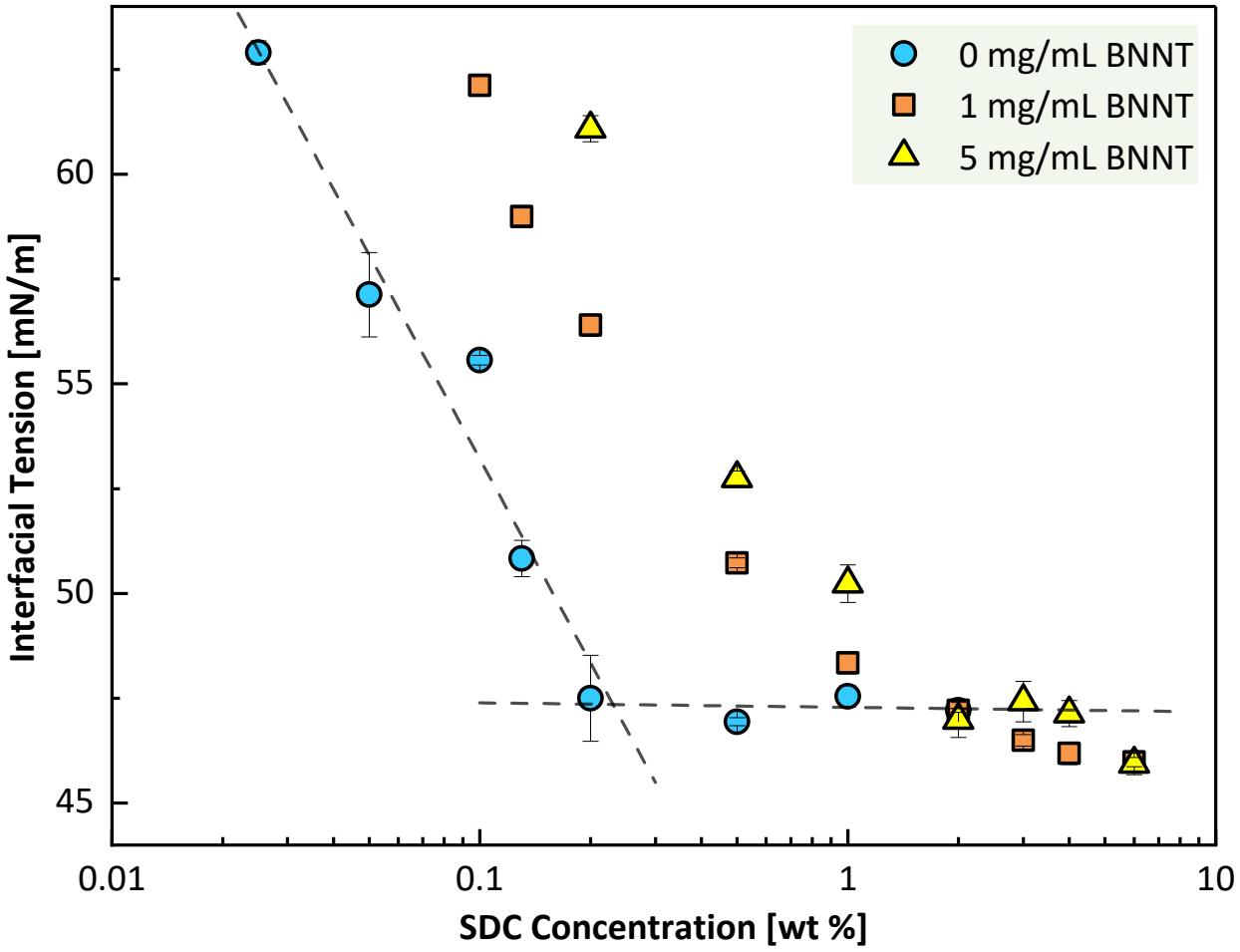

Figure S17. Interfacial tension measurements of SDC solutions in the presence and absence of HP-BNNTs obtained using the pendant drop method. Dashed lines (--) represent a linear fit of the data points collected for SDC solution without BNNTs (0 mg/mL).

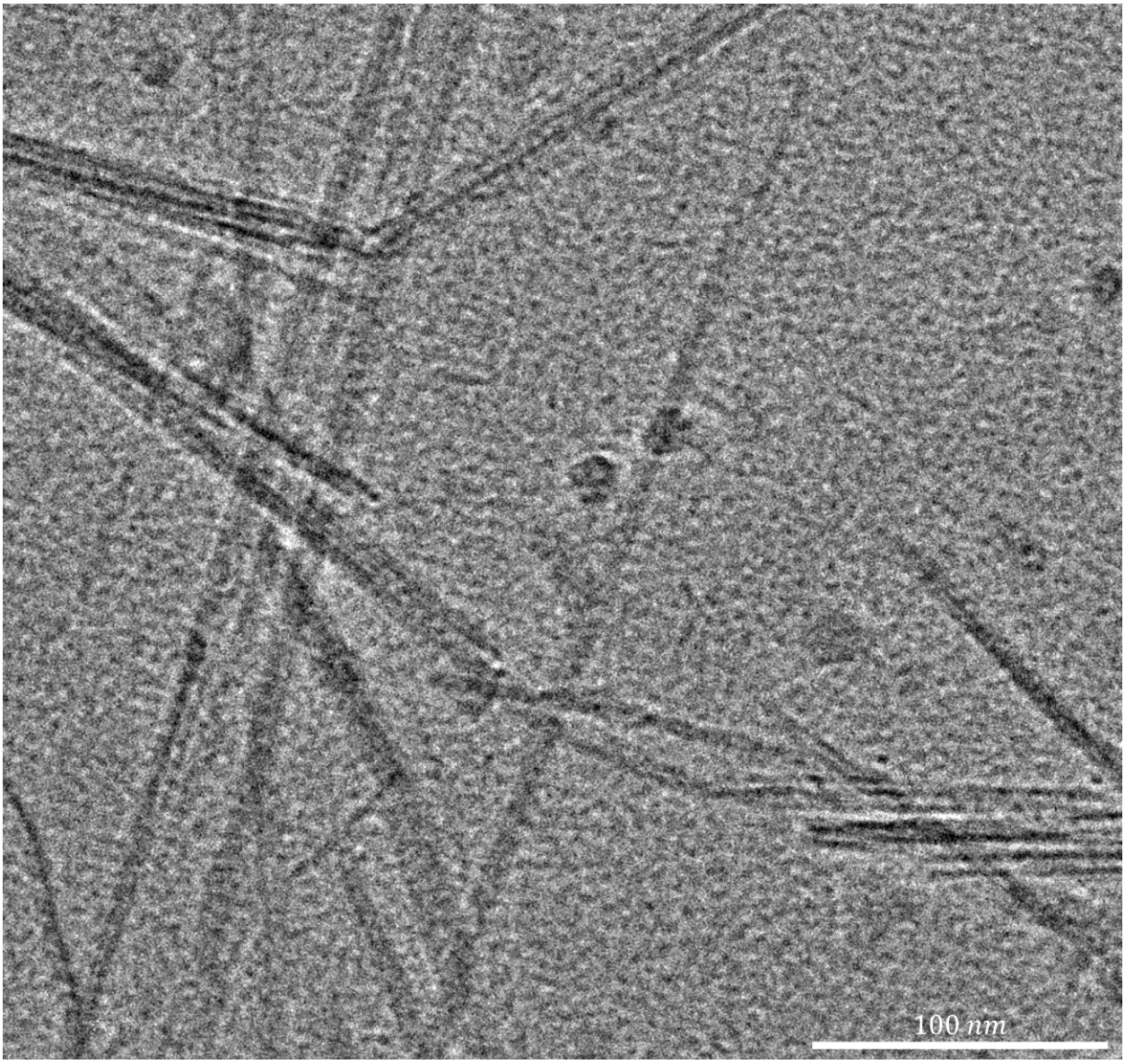

Figure S18. Cryo-TEM image of 0.05 wt % HP-BNNT in 1 wt % SDC, showing SDC globular micelles coexisting with SDC-coated BNNTs promoting their individualization.

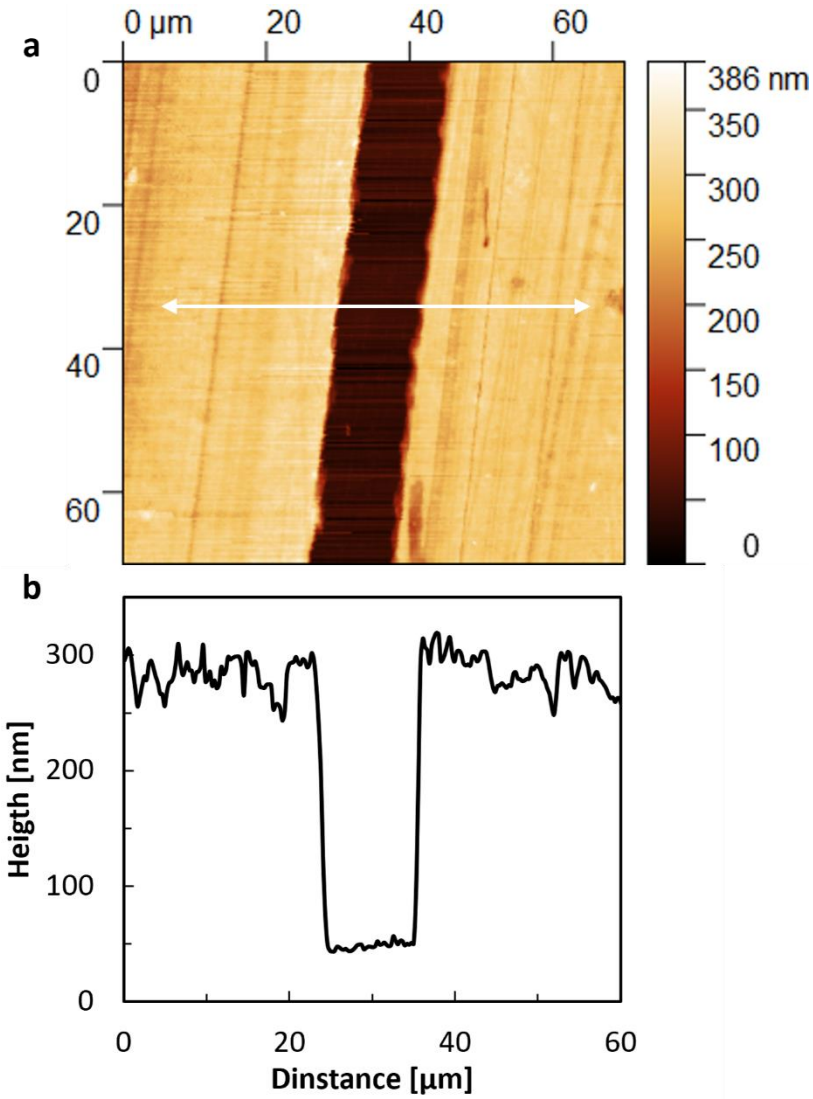

Figure S19. (a) AFM topographic image of the BNNT film. (b) Height profile along the double-headed arrow shown in (a), used to determine film thickness.

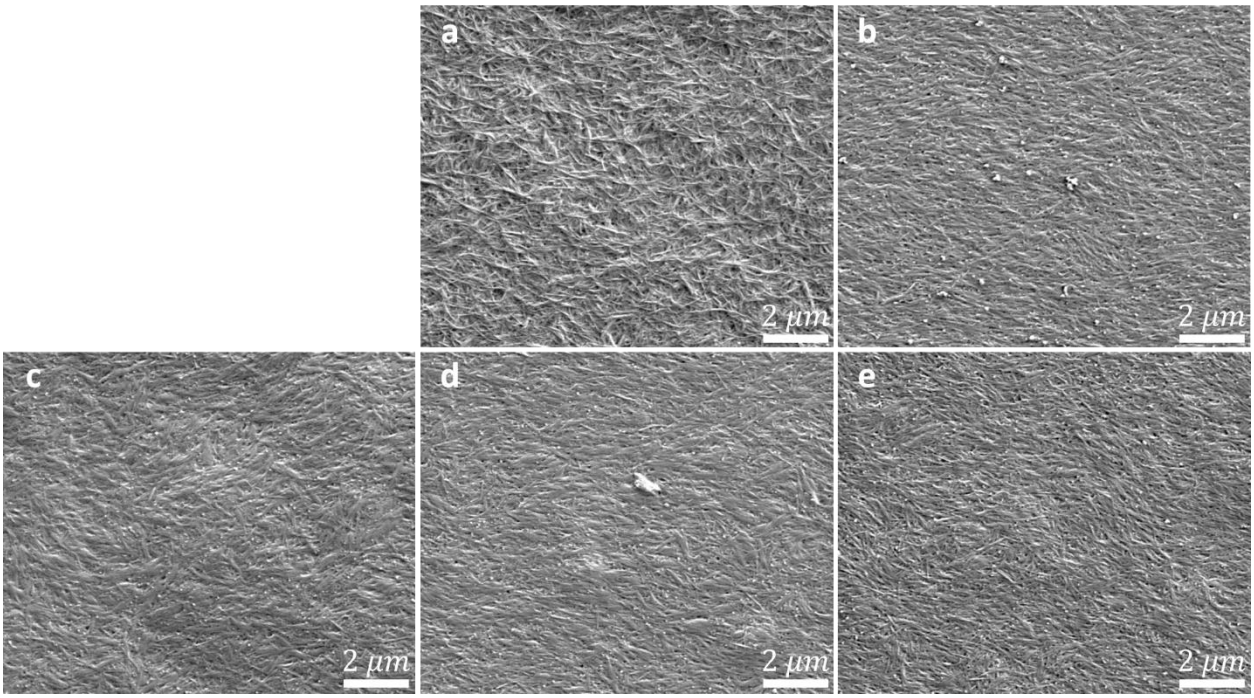

Figure S20. SEM micrographs of BNNT films prepared using doctor-blade and treated under different conditions: (a) film immediately coagulated in IPA, showing a loss of alignment from the LC dispersion. (b) film immediately coagulated in chloroform, maintaining alignment from the LC dispersion. (c) film dried in air without coagulation, showing large domains of aligned BNNTs. (d) and (e) films were dried in air for 5 minutes at room temperature then coagulated in IPA and chloroform, respectively, showing improved alignment over immediate coagulation.

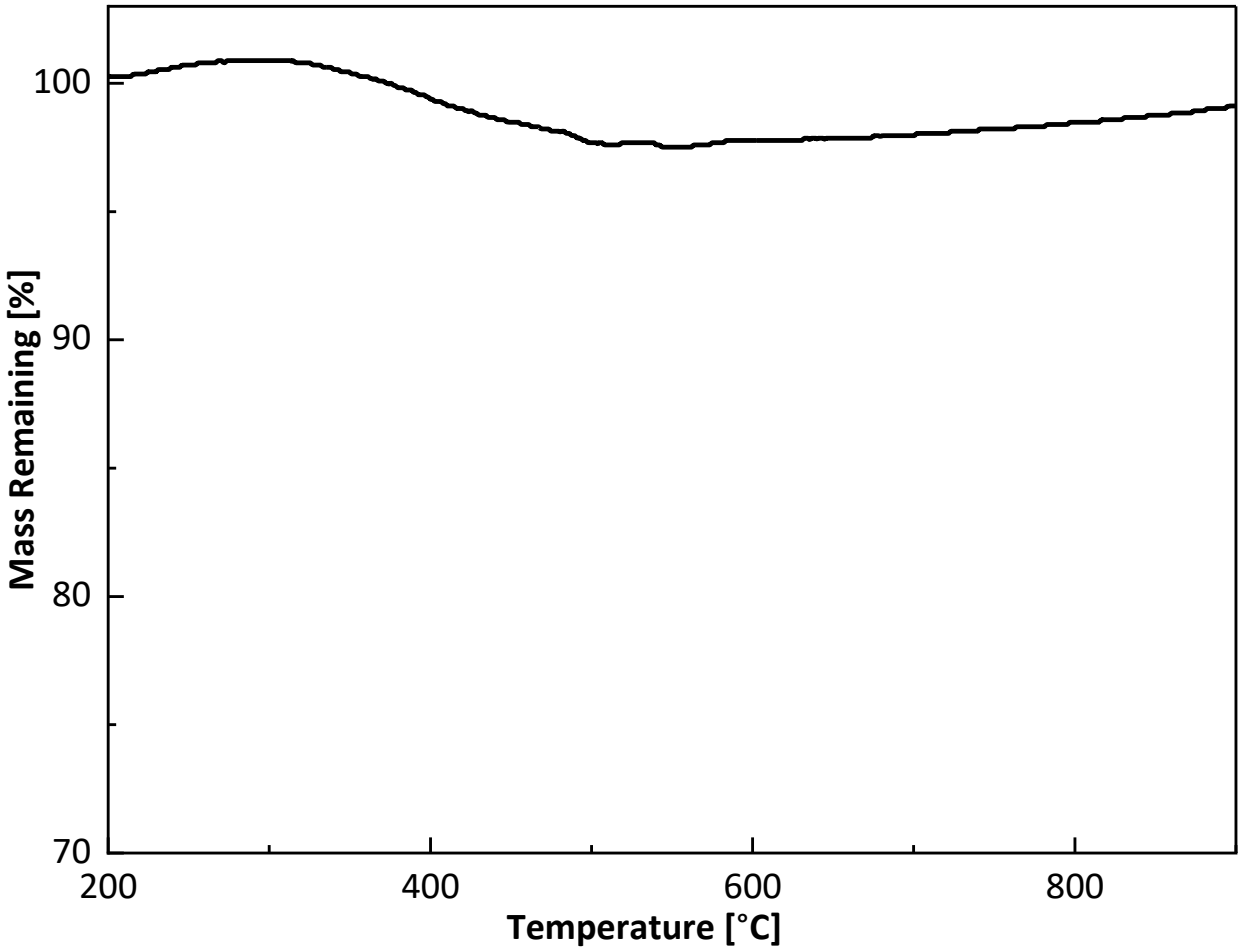

Figure S21. TGA of a BNNT film, indicating a surfactant content of approximately 3% of the total film mass. The analysis also demonstrates the thermal stability of the film up to 800 °C.